Final author comment on "High stresses stored in fault zones: example of the Nojima fault (Japan)" *by* Anne-Marie Boullier et al.

Anne-Marie Boullier[1], Odile Robach[2], Benoît Ildefonse[3], Fabrice Barou[3], David Mainprice[3], Tomoyuki Ohtani[4], Koichiro Fujimoto[5]

[1]ISTerre, Univ. Grenoble Alpes, CNRS, 38000 Grenoble, France
[2]CEA, INAC-MEM, Univ. Grenoble Alpes, 38000 Grenoble, France
[3]Géosciences Montpellier, CNRS, Univ. Montpellier, 34095 Montpellier, France
[4]Gifu University, Department of Civil Engineering, Gifu 501-1193, Japan
[5]Faculty of Education, Tokyo Gakugei University, Tokyo, Japan

Correspondence to: Anne-Marie Boullier (anne-marie.boullier@univ-grenoble-alpes.fr)

We received two comments by referees. We thank both of them for their carefull review and helpful comments allowing us to precise and further discuss our results.

Final response to the first referee

Here below, we answer to F. Aben's comments (se-2017-130-RC1).

Mechanisms of dynamic damage

F. Aben's first comment : *"The results of this paper show that high enough strain rates for pervasive dynamic damage are reached at greater depth, and that compressive stresses are stored. Also, there are independent strain measurements, including directions, from the biotite (compres- sional) and the opening of veins (extensional). Even more, the sample's distance from the fault is very substantial (51.3 m) and outside the range of higher strain rates produced by 'normal' earthquake ruptures. Although the results of one sample cannot answer such a question unequivocally, it would be interesting to see the authors' view on the loading mechanism or rupture mechanism that can produce such dynamic damage nonetheless. »*

Answer : Let us first resume our main observations. Compressive microstructures (alignments of tiny fluid inclusions in quartz, kink-bands in biotite) correspond to a compression perpendicular to the Nojima fault, and to less than 5% shortening. High stresses or strain-rate plastic deformation of quartz is synchronous with the compressive microstructures. Extensive microstructures are E-W orientated laumontite-sealed mode I veins corresponding to a N-S extension and to an average of 10 to 20% extension as measured using the width of laumontite veins. There is almost no shear deformation observed in that sample except the type 1 breccia-like veins which are trans-tensional E-W orientated features. On the basis

of crosscutting relationships, we propose that the compressive microstructures appear before the extensive ones. All these deformations are interpreted as dynamically induced 51.3 m away from the Nojima fault. Moreover, we have suggested that they have formed during a single seismic event on the Nojima fault. We are aware that this is a very strong assumption and after discussion with a seismologist (Michel Bouchon) we have changed our mind on that point: the laumontite veins may have formed during several successive so-called characteristic earthquakes . Actually, earthquakes are repeating on a fault and have similar characteristics. Therefore, successive similar earthquakes may induce successive similar damage.

Do these observations provide information on the loading mechanism at the origin of the dynamic damage? Several processes have been recently proposed in the literature for explaining shallow damage zone pulverization (see review in Aben et al., 2017): dynamic compressive loading, dynamic tensile loading, fluid-assisted decompression, wrinkle-like pulses and super-shear, as listed in F. Aben's comment.

Experiments reproducing compressive loading using Split-Hopkinson bars has produced microstructures qualitatively similar to those observed in the described sample. Thus, as suggested in our paper, compressive loading is a good candidate in our case. Experiments reproducing tensile loading are more difficult to realize (see review in Zhang and Zhao, 2013) and require specific sample shapes. These experiments reproduce simple fractures rather than pulverization (Zhang and Zhao, 2013). No microstructural analyses are available for comparing with the microstructures in the Nojima sample. Nevertheless, we have to keep in mind that dynamic tensile strength is lower than dynamic compressive strength (Zhang and Zhao, 2013).

The fluid-assisted decompression model corresponds to hydrofracturing due to a sudden drop of fluid pressure in the rock. If this mechanism may be efficient in high permeability sedimentary rocks present in the subsurface, it appears highly improbable in the case of the Nojima granodiorite, which has a very low permeability (10^{-8} to 10^{-9} darcy under 50MPa confining pressure, Lockner et al., 2009).

Considering the model of wrinkle-like pulses related to a bimaterial interface (Shi and Ben-Zion, 2006), it is not appropriate in the present case because both foot-wall and hanging-wall of the Nojima fault are constituted by the same granodiorite and the profile of physical properties of rocks across the fault is symmetrical (Lockner et al., 2009). Moreover, this model does not apply at great depth (> 3 km, Ben-Zion and Shi, 2005) where dynamic damage has been demonstrated to occur in the Nojima sample on the basis of laumontite in the veins and microfractures.

The last model is the supershear, i.e., a rupture front propagating faster than the S-wave velocity (Bouchon et al., 2001) and the formation of a Mach-cone (Rosakis et al., 2007). If supershear is mostly observed during high magnitude earthquakes along simple large faults (Bouchon and Vallée, 2003), it may also occur along smaller linear segments (see review in Rosakis et al., 2007). It triggers damage laterally and also in depth (Bouchon and Karabulut, 2008). Thus, supershear could be invoked for inducing the dynamic damage at 51.3 m from the Nojima fault and at 3.7 - 11.1 km depth. Depending on the location of the rupture source and the direction and velocity of rupture propagation, the walls of the fault may be either tensile or compressive whatever the far-field tectonic stress configuration. It has to be pointed out also that the peak dynamic stress is much higher than the static stress and may trigger fracturing and damage at a large distance to the fault

(Brodsky and Prejean, 2005). Thus, all these considerations may explain the occurrence of E-W orientated mode I cracks in the studied sample, an orientation which is not consistent with the far-field tectonic setting of the fault (left-lateral wrench fault with N-S compression, Famin et al., 2014).

To conclude, we argue that microstructures we observed in the unique but representative sample studied in this paper are due to dynamic damage. However, suggesting a unique mechanism for explaining this dynamic damage would be over-interpretating our data. We believe that additional studies are necessary including microstructural observations of orientated samples across the Nojima fault, including samples outside and inside the damage zone.

Correction added to the paper: We have added a section in our paper reproducing the above discussion:

7.6 Implications on the dynamic damage mechanism.

Residual stresses

F. Aben's second comment : *"The term residual stress is mentioned throughout the manuscript (starting at line 16, page 2). At line 20 (page 9) it becomes clear that the residual stress is a deviatoric residual stress (or Von Mises stress), calculated from residual deviatoric strain (line 2, page 9). It would help the reader if it is stipulated much earlier onward in the manuscript that a residual deviatoric stress is recovered from the sample, for instance in the introduction."*

Answer : Let us clarify some points. The residual stress is a term used in material sciences and may be defined as the stresses remaining in a solid when all the applied stresses have been removed. They may also be called internal stresses but we use "residual stress" as this term was used in former studies related to X-ray Laue micro-diffraction (Chen et al., 2011, 2015; Kunz et al., 2009). Residual stresses are investigated in solids or structures in order to evaluate their reaction to specific loading conditions. Similarly, behaviour of rocks submitted to quasi-static or dynamic loading will depend on their loading history and residual stresses.

In the present case as in the other examples in the literature (Chen et al., 2011, 2015; Kunz et al., 2009), the elastic strain tensor is determined by X-ray Laue micro-diffraction (our Fig. S6) from the deformation of the crystal lattice (b/a, c/a, α, β, γ) compared to an undeformed lattice. This give us the deviatoric elastic strain ($\varepsilon_{xx} + \varepsilon_{yy} + \varepsilon_{zz} = 0$). The residual stress tensor is calculated by applying the Hooke's law on the elastic strain tensor and thus, we have access to the deviatoric stresses. The von Mises or equivalent stress is in turn calculated from the residual stress tensor (our formula 3) and is a convenient scalar to illustrate the stress state at each point of a map. As pointed out by the second referee, due to the low symmetry of quartz, the calculated von Mises stress is an approximate. However, as the largest error is 24 MPa, we keep it as is for simplicity (see response to second referee below).

For the same reason of simplicity, we prefer to use the general term stress or residual stress throughout the paper for discussing stresses in general, except when we calculate and discuss the deviatoric stress tensor from the deviatoric elastic strain tensor (sections 6.2 and 7.4).

Corrections added to the paper: We have clarified that point in our paper. We also have taken into account the comments made by the second referee pointing out that the deviatoric stress and Von Mises stress obtained from deviatoric strain measurements are only approximate (see Supplementary Material SM7 for an evaluation of the error) due to the trigonal structure of the quartz lattice.

F. Aben wrote : *"Following this, the sentence at lines 6-9 (page 13) on the confining pressure at depth causing the residual stress becomes redundant, since this is the lithostatic and not the deviatoric component by definition."*

Answer: The F. Aben's comment suggests that he misunderstood our point and, therefore, that we should clarify and rewrite that section. We ask the question: "How such large residual stresses may be preserved in such a small volume for such a long time?" One could argue that the residence of the sample at depth, i.e., under confinement, could have preserved the residual stresses in the quartz grains. In this case, these residual stresses should have been released during sample recovery by drilling and during sawing and thinning for thin section manufacturing. Therefore, confinement at depth is not a sufficient reason for preserving residual stresses. As pointed out later in the paper (page 12, lines 13-15), we guess that dislocation density is high in the studied quartz crystals because of the high stress and strain-rate conditions of deformation. More importantly, dislocations are probably entangled and mostly immobile due to the low temperature (<300°C). This could be compared to work hardening in metals: high density of entangled dislocation inhibits dislocation gliding. Therefore, recovery, and stress release cannot occur. To conclude, the low temperature rather than the confining pressure allows the conservation of the residual stress in the sample.

Corrections added to the paper : We have rewriten the sentence.

Other specific comments

- *Line 27, page 2 : « The threshold recorded by Doan & Gary is a strain rate threshold. Using linear elasticity, such a strain rate threshold can be transformed into a stress rate threshold, although elastic properties are weakly rate dependent in this regime. »*

We agree and have replaced « shear stress threshold » by « strain-rate threshold »

- *Line 28-30, page 2: « On the Yuan paper. Maybe the authors can add here something like: With increasing confining pressures, the strain rate threshold increases as well. »*

We accept the suggestion and have added the proposed sentence.

- *Line 5, page 3 : Comment on the paper by Sagy and Korngreen (2012).*

We agree and have replaced « pulverized » by « dynamically fractured » as suggested.

- *Recent paper by Sullivan and Peterman (2017).*

We thank F. Aben for the information and added this interesting reference as an exemple of pulverization at depth.

- *« The fact that only one thin section is subjected to in-depth analysis can be mentioned earlier, for instance in the introductory paragraph of section 3.1. »*

We agree and mention that at the end of the introduction when listing the techniques: « Electron Back Scattered Diffraction (EBSD) and X-ray Laue microdiffraction were used to characterize the intragranular heterogeneities of crystallographic orientation in quartz grains, and to map the elastic strains and residual stresses. The complexity of the later technique is the reason for studying a unique but representative sample in detail."

- *«What is the meaning of A exactly in line 6, page 12? »*

We have precised : « A is a dimensionless constant of proportionality which is approximately equal to 4 for many materials"

- *« A question raised by the observations of stressed sub grains due to ductility (dislocations) and the microfractures is: Would such residual stress be released by microfracturing in the vicinity? Are there geometrical relations that would show (or not show) such a relationship between the two microstructural expressions of damage ? »*

First, we apologize for a mistake in our manuscript. Figures A2 and A3 have to be exchanged (but not the captions).

If we consider the elastic strain (Figure A3c) and the microstructures of this area (Fig. 10a), we may observe that microfractures are superimposed to zones of high elastic strain gradients, and thus, to high residual stresses that have not been removed from the sample. On the contrary, elastic strain variations between microfractures are smoother. But given the small size of the studied sample, we cannot assert that there is a relationship between the two microstructural expressions of damage.

- *« The residual peak stress of 100 MPa and mean stress of 141 MPa mentioned in the manuscript … is confusing. »*

We agree and thanks F. Aben. This sentence has been replaced by :

« The distribution of the filtered von Mises stress displays a modal value at 100 MPa for a mean at 141 MPa."

- *« Line 11 and 12, page 15, on the drop of P-wave velocity. Such a stress drop is not an exclusive indicator for dynamic damage, merely an indicator for an increase in damage (however it has been created). Therefore, this statement is over interpretation. »*

This is exact and we have modified the text consistently : « Such a 7% decrease in V_P velocity is another indicator for unvisible damage in the sample whatever the dynamic or quasi-static origin of the damage."

- We have also added a reference (Stünitz et al., 2017) that describe deformation of fluid inclusions in quartz and confirms the orientation of alignments of neonate inclusions perpendicular to the maximum compressive stress.

Response to "Technical comments" by F. Aben (RC1-supplement).

First, we have checked our text and splitted the « complicated » or « too long sentences » for improving the manuscript.

We sincerely thank Frans Aben for these technical comments who have facilitated the correction of our manuscript.

- Line 31, page 2: Please remove *Actually and*

Done

- Line 1, page 3: Add *off-fault* between *co-seismic damage*.

Done

- Line 9, page 3: Replace *brought to the near surface* with *exhumed*?

Done

- Line 22, page 3: Add *the* between *almost entire*.

Done

- Line 22, page 3: Replace *due to the cohesion* by *,thanks to the cohesion of*

Left as it is

- Line 26, page 3: Replace *was characterized* by *is evidenced Final*

Left as it is.

- Line 27, page 3: Add *of the fractures* after *main sealing mineral*.

Done

- Line 28, page 3: Replace *(Cho et al., 1987), which* by *(Cho et al., 1987). This*

Done

- Line 13, page 4: Replace *thin (100 µm thick) sections* by *thin sections (100 µm thick)*

Done

- Line 5, page 5: Replace *is* by *was*.

Done

- Line 6, page 5: Replace *are* by *were.*

Done

- Line 7, page 6: At the description of the intragranular microfractures oriented at 50°N, maybe add that this direction is also independent from crystallographic orientation (similar to line 14 in the same section).

Done

- Line 18, page 6: Reference?

These are our own unpublished observations. The sentence has been modified.

- Line 20, page 6: Reference?

We have added the reference to Tanaka et al. (2001)

- Line 30, page 8: I recommend not to use the term *experimental* here, it implies experimental work. Replace by for instance: *measured*

Done

- Line 17, page 10: remove comma after *thus.*

Done

- Line 27, page 10: Change *sriking* into *striking*

Done

- Line 26, page 11: Replace *actually* by *even more*

Done

- Line 5, page 12: Replace *alteratively* by *alternatively*

The sentence has been changed.

- Line 33, page 14: Replace *and* between the Aben and Dor references by a comma.

Done

- Line 27, page 15: Do the authors mean dissolution-precipitation processes?

Yes, modification done.

- Figure 13b: I recommend changing the x-axis labels to 100, 200, etc. for clarity.

Done

- Figure 1: It might be useful to add a little map of Japan as a large-scale reference. Also, add the name Ryoke to the granitiods in the legend.

Done

Final response to the second referee

We thank the second referee for pointing out some important points concerning Laue X-ray microdiffraction. Here below, we answer to his comments.

Comment 1 : *"Residual stresses are calculated from elastic strain measured by X-ray Laue microdiffraction and stress peaks at 100 MPa (mean 141 MPa)." In fact the "residual stress" should be explained and discussed in several aspects. It should be emphasized that the measured strain was actually deviatoric strain tensor, but the full strain tensor. Therefore, the stress tensor calculated was neither full stress tensor nor deviatoric stress tensor, and thus the so-called von Mises stress is not the real von Mises stress. How different could it be? A discussion would be appreciated.*

Answer : We agree with that and will provide an estimate of the error committed on the von Mises using this approximation in a supplementary material.

Correction in the text: Supplementary material 7 has been added and presents an evaluation of the error due to this approximation (maximum error 24 MPa). For simplicity, we use the term "Von Mises stress" in the paper as a shortcut for "pseudo Von Mises stress calculated from deviatoric strain".

Comment 2 : *"Quartz has trigonal symmetry, which leads to some possible ambiguity for the Laue pattern indexing, as shown in some reference papers, for example Journal of Applied Crystallography, 45, 982-989, DOI: 10.1107/S0021889812031287, 2012. Thus more details about how LaueTools handle such problem are welcome.*

Answer : We have added an appendix A2 about this issue in the paper. The ambiguity between the two variants of the Dauphiné twins (Chen et al., 2012) was not lifted in the previous 2-spots analysis, the map being located mostly in a single variant. The small domain of Dauphiné twin detected by EBSD in the region of the micro-Laue map is clearly visible in the micro-Laue map when mapping the maximum intensity of the second spot. We have checked our indexing of the spots based on the relative intensities of the various HKL spots and corrected Fig. 2b consequently. Thanks to the referee for pointing this.

Correction in the text : Appendix A2 has been added.

Comment 3 : *Page 16. "Indeed, although in theory a multi-grain indexation procedure could be applied to the multi-spot Laue pattern, in order to individually index each sub-spot present on the beam path, in practice the corresponding code for closely-spaced sub- spots is still unavailable." This is not real. The code is available and practical in many Laue data analysis software packages.*

Answer : Thanks for pointing this. Indeed automated indexation of all the sub-grains in a pattern with spots split into closely-spaced sub-spots (such as the spot shown in zoom 2 of Fig. 2c), is usually beyond the reach of serial analysis softwares designed to treat a whole map automatically : the tolerance needed at the indexation stage to accommodate the difference between the unstrained reference pattern and the (real) strained pattern leads to ambiguities when trying to link distant sub-spots each belonging to a group of sub-spots.

Correction in the text : No change in the text.

Comment 4: *Page 26. "especially the [02-22] spot". Square brackets are improper.*

Answer : This has been corrected.

References

Aben, F. M., Doan, M. L., Gratier, J.-P., and Renard, F. : Coseismic damage generation and pulverization in fault zones: Insights from dynamic Split-Hopkinson pressure bar experiments, in: Fault zone dynamic processes: evolution of fault properties during seismic rupture, edited by: Thomas, M. Y., Mitchell, T. M., and Bhat, H. S., Geophysical Monograph, John Wiley & Sons, Inc., 2017.

Ben-Zion, Y., and Shi, Z. : Dynamic rupture on a material interface with spontaneous generation of plastic strain in the bulk, Earth Planet. Sci. Lett., 236, 486–496, doi:10.1016/j. epsl.2005.03.025, 2005.

Bouchon, M., Bouin, M.-P., Karabulut, H., Toksoz, M. N., Dietrich, M. and Rosakis A. J. : How fast is rupture during an earthquake? New insights from the 1999 Turkey earth- quakes, Geophys. Res. Lett., 28, 2723–2726, 2001.

Bouchon, M. and Karabulut, H. : The aftershock signature of supershear earthquakes, Science, 320, 1323-1325, doi:10.1126/science.1155030, 2008.

Bouchon, M. and Vallée, M. (2003), Observation of long supershear rupture during the magnitude 8.1 Kunlunshan earthquake, Science, 301(5634), 824–826, doi:10.1126/science.1086832, 2003.

Brodsky, E. E. and Prejean, S. G. : New constraints on mechanisms of remotely triggered seismicity at Long Valley Caldera, J. Geophys. Res., 110, B04302, doi:10.1029/2004JB003211, 2005.

Chen, K., Dejoie, C., and Wenk, H.-R.: Unambiguous indexing of trigonal crystals from white-beam Laue diffraction patterns: application to Dauphiné twinning and lattice stress mapping in deformed quartz, J. Appl. Crystallogr., 45, 982-989, 10.1107/S0021889812031287, 2012.

Chen, K., Kunz, M., Tamura, N., and Wenk, H.-R. : Evidence for high stress in quartz from the impact site of Vredefort, South Africa, Eur. J. Mineral., 23, 169–178, doi:10.1127/0935-1221/2011/0023-2082, 2011.

Chen, K., Kunz, M., Tamura, N., and Wenk, H.-R.: Residual stress preserved in quartz from the San Andreas Fault Observatory at Depth, Geology, 43, 219-222, 2015.

Famin, V., Raimbourg, H., Garcia, S., Bellahsen, N., Hamada, Y., Boullier, A.-M., Michon, L., Revil, A., Uchide, T., Ricci, T., Hirono, T., and Kawabata, K.: Stress rotations and the long-term weakness of the Median Tectonic Line and the Rokko-Awaji segment, Tectonics, 33, 1900-1919, 10.1002/2014TC003600, 2014.

Kunz, M., Chen, K., Tamura, N., and Wenk, H.-R.: Evidence for residual elastic strain in deformed natural quartz, Am. Mineral., 94, 1059-1062, 2009.

Lockner, D. A., Tanaka, H., Ito, H., Ikeda, R., Omura, K., and Naka, H.: Geometry of the Nojima Fault at Nojima-Hirabayashi, Japan - I. A Simple Damage Structure Inferred from Borehole Core Permeability, Pure Appl. Geophys., 166, 1649-1667, 2009.

Rosakis, A. J., Xia, K., Lykotrafitis, G. and Kanalori, H. : Dynamic Shear Rupture in Frictional Interfaces: Speeds, Directionality, and Modes, In: Treatise of Geophysics, Elsevier, 153-192, 2007.

Shi, Z., and Ben-Zion, Y. : Dynamic rupture on a bimate- rial interface governed by slip-weakening friction, Geophys. J. Int., 165, 469–484, doi:10.1111/j.1365-246X.2006.02853.x, 2006.

Stünitz, H., Thust, A., Heilbronner, R., Behrens, H., Kilian, R., Tarantola, A., and Fitz Gerald, J. D.: Water redistribution in experimentally deformed natural milky quartz single crystals—Implications for H2O-weakening processes, J. Geophys. Res.-Sol. Ea., 122, 866–894, 10.1002/2016JB013533, 2017.

Sullivan, W. A., and Peterman, E. M.: Pulverized granite at the brittle-ductile transition: an exemple from the Kellyland fault zone, eastern Maine, U.S.A., Journal of Structural Geology, 101, 109-123, 10.1016/j.jsg.2017.07.002, 2017.

Zhang, Q. B., and Zhao, J. : A review of dynamic experimental techniques and mechanical behaviour of rock materials, Rock Mech. Rock Eng., doi:10.1007/s00603-013-0463-y, 2013.

High stresses stored in fault zones : example of the Nojima fault (Japan)

Anne-Marie Boullier[1], Odile Robach[2], Benoît Ildefonse[3], Fabrice Barou[3], David Mainprice[3], Tomoyuki Ohtani[4], Koichiro Fujimoto[5]

[1]ISTerre, Univ. Grenoble Alpes, CNRS, 38000 Grenoble, France
[2]CEA, INAC-MEM, Univ. Grenoble Alpes, 38000 Grenoble, France
[3]Géosciences Montpellier, CNRS, Univ. Montpellier, 34095 Montpellier, France
[4]Gifu University, Department of Civil Engineering, Gifu 501-1193, Japan
[5]Faculty of Education, Tokyo Gakugei University, Tokyo, Japan

Correspondence to: Anne-Marie Boullier (anne-marie.boullier@univ-grenoble-alpes.fr)

Abstract. During the last decade pulverized rocks have been described on outcrops along large active faults and attributed to damage related to a propagating seismic rupture front. Questions remain on the maximal lateral distance from the fault plane and maximal depth for dynamic damage to be imprinted in rocks. In order to document these questions, a representative core sample of granodiorite located at 51.3 m from the Nojima fault (Japan) that was drilled after the Hyogo-ken Nanbu (Kobe) earthquake is studied by using Electron Back-Scattered Diffraction (EBSD) and high resolution X-ray Laue microdiffraction. Although located outside of the Nojima damage fault zone and macroscopically undeformed, the sample shows pervasive microfractures and local fragmentation. These features are attributed to the first stage of seismic activity along the Nojima fault characterized by laumontite as the main sealing mineral. EBSD mapping was used in order to characterize the crystallographic orientation and deformation microstructures in the sample, and X-ray microdiffraction to measure elastic strain and residual stresses on each point of the mapped quartz grain. Both methods give consistent results on the crystallographic orientation and show small and short wavelength misorientations associated with laumontite-sealed microfractures and alignments of tiny fluid inclusions. Deformation microstructures in quartz are symptomatic of the semi-brittle faulting regime, in which low temperature brittle, plastic deformation and stress-driven dissolution-deposition processes occur conjointly. This deformation occurred at a 3.7 – 11.1 km depth interval as indicated by the laumontite stability domain.

Residual stresses are calculated from deviatoric elastic strain tensor measured by X-ray Laue microdiffraction using the Hooke's law. The modal value of the von Mises stress distribution is at 100 MPa and the mean at 141 MPa. Such stress values are comparable to the peak strength of a deformed granodiorite from the damage zone of the Nojima fault. This indicates that, although apparently and macroscopically undeformed, the sample is actually damaged. The homogeneously distributed microfracturing of quartz is the microscopically visible imprint of this damage and suggests that high stresses were stored in the whole sample and not only concentrated on some crystal defects. It is proposed that the high residual stresses are the sum of the stress fields associated with individual dislocations and dislocation microstructures. These stresses are interpreted to be originated from the dynamic damage related to the propagation of rupture fronts or seismic

IST 12/1/18 10:47
Supprimé:

IST 12/1/18 10:48
Supprimé: that

IST 5/2/18 10:13
Supprimé: in

IST 5/2/18 10:13
Supprimé: a

IST 26/1/18 12:11
Supprimé: -

Anne-Marie Boullier 2/3/18 15:30
Supprimé: deviatoric

IST 10/1/18 16:43
Supprimé: and stress peaks

IST 10/1/18 16:43
Supprimé: (

IST 10/1/18 16:43
Supprimé:)

IST 23/1/18 16:02
Supprimé: damaged

IST 23/1/18 16:03
Supprimé: indicating

IST 23/1/18 16:01
Supprimé: highly

IST 12/1/18 10:51
Supprimé: ,

IST 12/1/18 10:56
Supprimé: and

waves at depth where confining pressure prevented pulverization. Actually, M6 to M7 earthquakes occurred during Paleocene on the Nojima fault and are good candidates for inducing this dynamic damage. The high residual stresses and the deformation microstructures would have contributed to the widening of the damaged fault zone with additional large earthquakes occurring on the Nojima fault.

1 Introduction

Using near-field seismic data recorded during earthquakes, it is possible to derive kinematic rupture models describing the spatial distribution of slip, rupture time and rise-time on the fault. Inversion of such models allows the determination of the space-time history of shear stress on the fault plane during the rupture. As an example, dynamic shear stress drop calculated for four well-instrumented large earthquakes on the San Andreas fault system varies from 20 MPa to 100 MPa (Bouchon, 1997). These values are very heterogeneous along the fault plane and can be regarded as a lower bound because of the limited spatial resolution of the kinematic models, which is at best a few kilometers. If the shear stress drop may be evaluated, the ordinary stress levels in the crust need to be measured in-situ in deep wells and boreholes by hydraulic fracturing technique and analysis of stress-induced well bore breakouts (Zoback and Healy, 1992) or by anelastic strain recovery measurements on cores retrieved from boreholes (Lin et al., 2006). Behaviour of a rock submitted to a tectonic (quasi-static) or seismic (dynamic) loading will depend on the loading history and residual stresses stored in the rock, which may be defined as the stresses remaining in the rock when all the applied stresses have been removed. Chen et al. (2015) measured up to 300 MPa residual stress in quartz fragments within the damage zone of the San Andreas fault at 2.7 km depth (*ca* 100 MPa confining pressure) using X-ray Laue microdiffraction. This residual stress value is higher than the ≈60 MPa differential stress deduced from in-situ measurements at 1671 m depth in the nearby SAFOD pilot hole (Hickman and Zoback, 2004).

Considering this high level of residual stress, large damage is expected in rocks surrounding a fault. Actually, when earthquake occurs, displacement is localized on a very thin (<10 mm) slip zone (Chester and Chester, 1998 ; Sibson, 2003) in which a gouge is formed by friction-related grain-size reduction (Sibson, 1977). Outside the fault core, 1 to 10^3 m wide zones may be damaged by brittle failure of the surrounding rocks. Recently, several examples of pulverized rocks lacking significant shear have been described at the surface or subsurface within 100 to 200 m wide bands close to large faults such as the San Andreas fault (Dor et al., 2006 ; Rockwell et al., 2009; Wechsler et al., 2011) or the Arima-Takatsuki Line in Japan (Mitchell et al., 2011), and have been attributed to dynamic co-seismic damage. At the same time, high strain-rate experiments on granite using Hopkinson bars without confinement have reproduced similar pulverized rocks (Xia et al., 2008) and predicted a dynamic strain rate threshold for pulverization (Doan and Gary, 2009). Below the pulverization threshold, fractures without shear are formed in the samples, which remain cohesive. Yuan et al. (2011) have performed similar experiments under confinement and did not observe pulverization under 132 MPa, which was the maximum confining pressure allowed by their apparatus. They suggest, therefore, that with increasing confining pressures, the strain

IST 12/1/18 10:57
Supprimé: associated to

IST 12/1/18 11:02
Supprimé: at a 3.7 – 11.1 km depth (laumontite stability domain)

IST 12/1/18 11:04
Supprimé: where confining pressure prevented pulverization.

IST 26/1/18 10:26
Supprimé: . ... [1]

IST 12/1/18 11:08
Supprimé: pre-earthquake and the

IST 5/3/18 11:22
Supprimé: For example, differential stress measured in the SAFOD pilot hole are ≈60 MPa at 1671m depth (Hickman and Zoback, 2004).

IST 5/3/18 10:52
Supprimé: This value is considerably lower than the

IST 5/3/18 10:52
Supprimé: measured by Chen et al. (2015)

IST 5/3/18 10:53
Supprimé: is the unique residual stress

IST 5/3/18 11:27
Supprimé: available in a damaged fault zone

IST 10/1/18 15:32
Supprimé: shear stress

rate threshold increases as well and that co-seismic pulverization process is restricted to the uppermost crust (≤ 3 km or ~100 MPa confining pressure; see review in Aben et al., 2017). Until now, pulverized rocks have been mostly observed at shallow levels although a few cases of co-seismic off-fault damage at depth are documented in the literature. Fragmentation of garnet at very high stresses and strain rates at depth corresponding to temperatures of about 300-350°C was first described by Trepmann and Stöckert (2002) in the Sesia Zone (Italian Alps). More recently, Sullivan and Peterman (2017) documented an example of granite pulverized at the brittle-ductile transition (400°C, 200 MPa) in the 50-200m wide damage zone of the Kellyland fault (eastern Maine, U.S.A.). Garnet fragmentation associated to pseudotachylites in the Western Norway eclogitic crust was attributed to deep crustal earthquakes (Austrheim et al., 2017). Concerning carbonate lithologies, Sagy and Korngreen (2012) described dynamically fractured rocks in a deep borehole at 5 km depth in Israel.

In this paper, we will investigate the natural deformation microstructures of a representative sample located in the hanging-wall of the Nojima fault zone (Japan). The studied sample was slightly deformed at depth, then exhumed by uplift and erosion, and collected by the Geological Survey of Japan in the Hirabayasdhi drillhole. We will compare the deformation microstructures of that sample with experimentally produced microstructures during dynamic loading and with naturally fragmented fault rocks described in the literature.

Techniques of petrographic microscopy, Scanning Electron Microscopy (SEM), cathodoluminescence (CL) were used to characterize microstructures, microfractures and their cement. Electron Back Scattered Diffraction (EBSD) and X-ray Laue microdiffraction were used to characterize the intragranular heterogeneities of crystallographic orientation in quartz grains, and to map the elastic strains and residual stresses. The complexity of the later technique is the reason for studying a unique but representative sample in detail. We will compare our results with those obtained by Chen et al. (2015) on a sample of the San Andreas fault zone. Then, we will discuss the significance of these results in terms of stress and strain-rate (quasi-static or dynamic), and the contribution of the observed microscopic damage to the widening of the damaged fault zone.

2 Geological setting

The Nojima Fault is a N45°-striking and 85° SE-dipping dextral reverse fault (Fig. 1) on which occurred the 1995 Hyogo-ken Nanbu earthquake (Kobe earthquake, M 7.2). The fault cuts across the Cretaceous Ryoke granodiorite. One year after the earthquake the Geological Survey of Japan (GSJ) successfully drilled the Hirabayashi borehole through the Nojima Fault on Awaji Island. Cores were recovered for almost the entire depth interval from 150 to 746.6 m due to the cohesion the rocks (Ito et al., 2000). The drillhole sampled the Principal Slip Zone (PSZ) of the Kobe earthquake at 624.5 m depth (Fig. 1c; Ohtani et al., 2000a; Tanaka et al., 2001). Two major periods of seismic activity on the fault separated by an exhumation of the basement of the Awaji Island were inferred using the relationships between hydrothermal minerals and deformation microstructures (Boullier et al., 2004a; Boullier, 2011). The first period of seismic activity was characterized by pseudotachylites and by laumontite as the main sealing mineral of the fractures. Laumontite is a zeolite ($Ca_4(Al_8Si_{16}O_{48})\cdot 18H_2O$) which crystallizes from aqueous fluids in the 100-300 MPa pressure range and at temperature

IST 10/1/18 14:23
Supprimé: Actually and until

IST 10/1/18 15:58
Supprimé: g

IST 10/1/18 15:48
Supprimé:).

IST 10/1/18 15:36
Supprimé: pulverized

IST 10/1/18 16:33
Supprimé: vicinity

IST 10/1/18 16:07
Supprimé:).

IST 12/1/18 11:35
Supprimé: 4-11 km

IST 12/1/18 11:34
Supprimé: during a first period of seismic activity on the Nojima fault dated from *ca* 56 Ma ago,

IST 10/1/18 14:24
Supprimé: brought to near surface

IST 12/1/18 11:37
Supprimé: at 220 m depth

IST 10/1/18 16:10
Supprimé: For microstructural observations,

IST 10/1/18 16:03
Supprimé: techniques

IST 10/1/18 16:03
Supprimé: ,

IST 10/1/18 16:34
Supprimé: k

IST 10/1/18 16:04
Supprimé: microfractures, their cement and

IST 11/1/18 14:53
Supprimé: residual stress

IST 10/1/18 16:35
Supprimé: as Chen et al. (2015) have done for a sample of the San Andreas fault zone.

IST 10/1/18 16:36
Supprimé: of the results

IST 11/1/18 14:44
Supprimé: a

IST 10/1/18 14:24
Supprimé: due

IST 11/1/18 14:44
Supprimé: b

lower than 300°C (Cho et al., 1987). This fixes the depth range of laumontite precipitation and laumontite-associated deformation to a 3.7 to 11.1 km depth interval using a rock density of 2.7 g/cm^3 and a lithostatic pressure gradient. This first period of seismic activity has been dated around 56 Ma by fission tracks in zircon (Murakami and Tagami, 2004). The second period (≤ 1.2 Ma) was characterized by carbonates precipitating in co-seismic fractures (Boullier et al., 2004b) and whose composition is consistent with the fluids circulating within the fault to day (Fujimoto et al., 2007). This two-stage tectonic history of the Nojima fault is compatible with the regional structural analysis (Kanaori, 1990 ; Fabbri et al., 2004 ; Famin et al., 2014), which reveals a sinistral wrenching in the Paleogene (65 to 23 Ma), followed by fault-normal extension in the Miocene (23 to 6 Ma) and a dextral slip active since the Plio-Quaternary (≤ 2 Ma).

In the present paper, we focus on deformation microstructures formed during the first period of seismic activity. The studied in a sample was in the 3.7 - 11.1 km depth range, as constrained by the laumontite stability field, before being exhumed and sampled at 220 m depth by the GSJ drillhole (Fig. 1c). By comparing conductive planes detected by the Fullbore Formation MicroImager (FMI, trademark of Schlumberger) with open fractures on 360° azimuthal core scanner images, it was possible to reorient most sections of the drillcore (Ohtani et al., 2000b). Therefore, microstructures observed in the studied sample could be geographically oriented, which is not usually the case.

3 Analytical procedures

3.1 EBSD

Small-scale observations were performed on polished thin sections (100 µm thick) cut perpendicular to the drill-core axis, *i.e.* close to the horizontal plane. Examination with a petrographic microscope was used to recognize the characteristic microstructural features and sealing minerals.

Crystallographic orientation of quartz was determined by indexation of electron-backscattered diffraction (EBSD) patterns using the Camscan Crystal Probe X500FE SEM (Géosciences Montpellier, CNRS, Université de Montpellier), equiped with EBSD HKL NordlysNano detector for crystallographic analysis and an EDS X-Max^N 20mm² detector for chemical analysis, both being driven by the AZtec software (Oxford Instruments). Diffraction patterns were generated at 20° tilted incident electron beam with a horizontal carefully polished thin section (note this equivalent to 70° tilt of conventional SEM). The orientation maps were obtained in automatic acquisition mode with a step size of 4µm or 0.5µm for detailed areas. Standard post-acquisition data processing was done using the Tango software of the Channel 5® suite (HKL Technology), to (i) remove isolated pixels that are indexed as a given phase and surrounded by either non-indexed pixels of pixels indexed for another phase, and (ii) fill non-indexed pixels that have a minimum of 6 neighbouring pixels with the same orientation, EBSD data processing was then performed using the MTEX open source matlab toolbox (version 4.3.1; http: //mtex-toolbox.github.io/; Hielscher and Schaeben, 2008; Bachmann et al., 2010: Mainprice et al., 2014).

IST 10/1/18 14:28
Supprimé: , which

IST 12/1/18 11:29
Supprimé:

IST 12/1/18 11:30
Supprimé: the

IST 12/1/18 11:30
Supprimé:

IST 8/3/18 15:20
Supprimé: which

IST 10/1/18 14:28
Supprimé: sections

IST 12/1/18 11:37
Supprimé:

3.2 Laue X-ray microdiffraction

Laue X-ray microdiffraction maps were collected on the same thin section as for EBSD using the synchrotron X-rays of a bending-magnet at the ESRF (Grenoble) and the apparatus of the CEA-CNRS CRG-IF BM32 beamline following a method described by Ulrich et al. (2011) and Robach et al. (2017). The 0.5 x 0.5 μm^2 polychromatic (5 to 22 KeV) horizontal X-ray beam impinges the sample surface inclined at 40° angle (Fig. 2a). The Laue patterns were collected on a MAR 165 CCD camera with 165 mm diameter and 2048 x 2048 pixels at 70 mm to the sample (Fig. 2b), mounted around a diffraction angle 2θ of 90° (in reflection geometry). The geometry of the diffraction experiment was calibrated using the Laue pattern of a Ge single crystal, as described in Ulrich et al (2011). The sample was scanned in front of the X-ray microbeam for mapping using a high-resolution x-y stage. Exposure time at each x-y point was 0.2 s. The probing depth in the investigated X-ray transparent material (quartz) was limited by the thickness (100 μm) of the thin section. Depending on the (x, y) position of the probe, quartz deformation, single spots (one cristallite) or multiple spots (several subgrains) were obtained (Fig. 2c). Automated analysis of Laue patterns comprises different stages that were described in Tamura (2014) for XMAS software and Robach et al. (2017) for LaueTools software (Micha et al., http://sourceforge.net/projects/lauetools/). Here LaueTools software was used for the Laue pattern indexation, determination of the crystal Euler angles (orientation) and the distorsion of the quartz unit cell (deviatoric elastic strain, obtained by comparing the experimental and the undeformed unit cell). The details of the data analysis are explained in the Appendix A1. As pointed out by Chen et al. (2012), when indexing the Laue spots, it is impossible to lift the ambiguity between a crystal and its Dauphiné twin (rotated by 180 degrees around c-axis) by using only the spot positions, and spot intensities need to be exploited (see Appendix A2 for details).

IST 10/1/18 14:30
Supprimé: is

IST 10/1/18 14:30
Supprimé: are

IST 8/3/18 15:27
Supprimé: by

4 Characterization of microstructures

The NOJ220 sample studied in this paper is a macroscopically undeformed granodiorite located outside the damage fault-zone at 220m depth in the borehole and a distance d_{fault} = 51.3 m to the fault plane in the hanging-wall (see Fig. 1c). It shows a typical isotropic magmatic structure and contains the following minerals: orthose, plagioclase, hornblende, biotite, cm-size quartz and accessory minerals such as zircon, apatite, titanite and allanite. Plagioclase, hornblende and biotite appear as gray, green and brown respectively on the thin section (Fig. 3a). Deformation microstructures are omnipresent when observed under the microscope. They are described below.

IST 8/3/18 15:45
Supprimé: crystals

IST 8/3/18 15:46
Supprimé: which

IST 8/3/18 15:45
Supprimé: cm-size quartz and by accessory minerals such as zircon, apatite, titanite and allanite.

4.1 Laumontite-filled veins

Two types of laumontite-filled veins are defined depending on their size. The first type is represented by wide (up to 1mm) and long (more than 3 cm, the thin section length) veins, which are indicated by yellow arrows on Fig. 3a. They are generally straight or slightly curved, and E-W striking and 70° southward dipping in the geographic frame. They contain large angular fragments of the granodiorite minerals embedded in small (<0.2 mm) laumontite crystals (Fig. 3b and 3c).

Fragments generally do not touch each other. Biotite fragments are delaminated, as are some biotite crystals immediately adjacent to the veins. The different nature and crystallographic orientation of the fragments compared to the fracture-wall minerals suggest that these fragments have been at least rotated and probably transported some distance from their initial position. The widest veins are clearly dilatant with some shearing component as shown by the deformed cleavages of neighbouring biotite crystals. However, the exact opening kinematics cannot be clearly established on the basis of the horizontal thin section alone. These veins may be qualified as "breccia-like" veins and are similar to those described by Blenkinsop and Sibson (1992, their Fig. 4d) in the core samples from the Cajon Pass drillhole near to the San Andreas Fault. The second type is represented by 20 – 200 µm wide and several cm long veins. They are transgranular, straight or with a jigsaw geometry, which are roughly E-W orientated and filled by laumontite prisms. They do not contain fragments and have parallel vein walls (thick black arrows on Fig. 4b; Si, Ca and Al maps in Fig. 4e). In these veins, the prisms of laumontite are generally orientated at high angle to the vein walls.

IST 11/1/18 15:30
Supprimé:

IST 8/3/18 15:50
Supprimé:

IST 8/3/18 15:50
Supprimé: y

IST 26/1/18 10:17
Supprimé:

4.2 Deformation microstructures in quartz

When observed under the petrographic microscope, quartz grains display a intracrystalline deformation characterized by undulous extinction without dynamic recrystallization. They are also pervasively affected by numerous intragranular microfractures (Fig. 4a) whose N50° orientation is independent from crystallographic orientation of the host quartz. They are only visible at a small scale (small black arrows in the grain investigated using EBSD, Fig. 4b) and are sealed by laumontite as shown on the Si, Ca and Al maps on Fig. 4e. Nevertheless, quartz grains have preserved their magmatic shape (Fig. 3a), thus indicating a low finite strain.

Fluid inclusions in quartz grains of the NOJ220 sample are unusual. Contrary to fluid inclusions in undeformed quartz-bearing rocks which have generally rounded or negative crystal shapes (Roedder, 1984), fluid inclusions define short (tens of µm) alignments of tiny neonate fluid inclusions (see Fig. S1). These alignments share the same N50° orientation parallel to the Nojima fault in all quartz grains independently of the crystallographic orientation of the host quartz (Fig. S1a). They form a continuum with the pervasive intragranular N50°-orientated healed microfractures, which share the same dark blue signature on the SEM-cathodoluminescence image and are themselves branched on laumontite-filled veins (see Fig. S2 and S3). Our observations indicate that the alignments of tiny fluid inclusions are present in most of the core samples within the 200 m to 750 m depth range in the GSJ drillhole.

IST 12/1/18 11:43
Supprimé: n

IST 11/1/18 15:04
Supprimé: N50° orientated

IST 10/1/18 14:32
Supprimé: , which

IST 12/1/18 12:48
Supprimé: independant

IST 10/1/18 14:40
Supprimé: The

IST 11/1/18 11:27
Supprimé: all

IST 11/1/18 11:15
Supprimé: .

4.3 Kink-bands in biotites

Kinking of (001) cleavage in biotite is a common feature in the NOJ220 sample and in most of the samples along the drillhole (Tanaka et al., 2001). Kink-bands are at high angle to (001) cleavage. They are comparable to kink-bands in biotite described in granitic samples from the shock region around a nuclear explosion (Cummings, 1965 ; Fauré, 1970) or in granite deformed under quasi-static conditions (Amitrano and Schmittbuhl, 2002). They provide a marker to extract the shortening intensity by measurement of the change in length of (001) cleavages, and the direction of compression by

IST 11/1/18 11:16
Supprimé: as

IST 11/1/18 11:26
Supprimé: all

IST 26/1/18 10:09
Supprimé: a

IST 26/1/18 10:09
Supprimé: and

measuring the orientation of kink-bands (Fig. S1b). Strain recorded by biotite in the NOJ220 sample reaches up to 5%. Kink-bands are roughly N50° orientated parallel to the alignments of tiny fluid inclusions described above (Fig. S1a) and to the Nojima fault.

5 EBSD measurements in quartz

The first quartz grain investigated using EBSD (Fig. 4) is representative of the average density of microfractures in the NOJ220 sample. The misorientation map (*i.e.* misorientation of each pixel relative to the mean orientation of the grain, Fig. 5b) shows a chessboard pattern defined by large (50-100 μm) subgrains limited by sharp boundaries which are mostly independent of the microfracture geometry. Smaller misorientation domains are superimposed on this chessboard pattern and are roughly elongated parallel to the microfractures (lower right area in Fig. 5b), but are cross-cut by them in many places. Misorientation axes for subgrain (either large or small) boundaries showing 0.5° to 5° misorientation are preferentially around the (0001) axis (Fig. 5d). Dauphiné twinning characterized by a rotation of 60° around (0001) is shown on the map of Inverse Pole Figures of the X axis (IPF X, Fig. 5a) by the small dark green domains. On the pole figures (Fig. 5c), they are characterized by the superposition of (10-11) and (01-11) in twinned and untwinned domains when (11-20) and (10-10) remain the same (*e.g.* Mainprice et al., 1993). Note that the Dauphiné twinned domains are also slightly elongated in N50° direction similar to that of the intragranular microfractures.

Microfractures may be locally very dense as in the N50° to N90° orientated array joining one biotite or hornblende to another across the whole thin section (Fig. 6). Figure 7 shows a group of quartz grains along this array which is squeezed in between a biotite and an amphibole, and cut by numerous microfractures radiating in a Hertzian pattern and sealed by laumontite (Ca, Al and Si maps in Fig. 7c). Up to 30% dilatancy was measured on the SEM image (Fig. 7b) by cumulating the thicknesses of laumontite-filled microfractures on a transect perpendicular to them. This dilatancy may be compared to the average value of 10% extension measured in several quartz grains. Alignments of tiny fluid inclusions in the neighbouring quartz have a strong N50° orientation and display the same dark-blue cathodoluminescence signature as the healed microfractures which are themselves in continuity with the laumontite-sealed microfractures (see Fig. S3). Only the quartz grains were selected for the EBSD map. EBSD measurements of the three quartz grains reveal Dauphiné-twinned domains (Fig. 8a) showing the same crystallographic relationships as in the previous example (see pole figures in Fig. 8c), and misorientation domains (Fig. 8b). As for the quartz grain investigated in Fig. 5, large subgrains define a chess-board pattern independent of the microfracture geometry. Superimposed smaller misorientation domains are roughly elongated parallel to, but cross-cut by the microfractures. Misorientation angle relative to the mean reaches up to 10° in this area (Fig. 8b) compared to the 5° misorientation in the mildly microfractured quartz mapped in Fig. 5b. Rotation axis of subgrain boundaries showing > 0.5° misorientation is again preferentially around [0001] (Fig. 8d). However, pole figures (Fig. 8c) do not show significant dispersion of crystallographic axes around [0001]. The three components of rotation (Rx, Ry and Rz) were calculated using the EBSD data and the Laue Tools Package (Fig. 9, see Supplementary Material SM4 for

IST 12/1/18 11:49
Supprimé:

IST 8/3/18 15:56
Supprimé: and

IST 8/3/18 15:56
Supprimé: k

IST 12/1/18 12:47
Supprimé:

IST 6/3/18 15:31
Supprimé: ;

IST 12/1/18 12:48
Supprimé: independant

IST 15/1/18 10:19
Supprimé: and

IST 15/1/18 10:19
Supprimé: o

IST 8/3/18 16:05
Supprimé: of

mathematical transformations applied to the EBSD data in order to pass the orientation matrices and map points positions into the LaueTools sample reference frame). They indicate that neighbouring fragments did not rotate greatly relative to each other (2° to 5°) during fragmentation. Actually, Rx component (max. 30 mrad or 1.72°) is slightly lower than Ry (max. 64 mrad or 3.67°) and Rz (max. 90 mrad or 5.15°).

6 Elastic strain and residual stress

In order to characterize the small misorientation domains and the damage related to microfracturing, a small area of the representative quartz grain studied in Fig. 4 and 5 (see location on Fig. 4b and 5b) was investigated in detail using EBSD and X-ray Laue microdiffraction.

6.1 Orientation map

A high resolution EBSD map was performed with a 0.5 µm step and misorientation to the mean orientation was calculated (Fig. 10b). As already observed in Fig. 4c and 4d, two types of intracrystalline deformation features are observed: (i) large 50 to 100 µm wide sub-grains limited by sharp straight or slightly curved sub-grain boundaries (Fig. 10b) with 0.5° to 1° misorientation indicated by large steps on the misorientation profile (Fig. 10c), and (ii) small elongated sub-grains within the large ones, NNE-SSW orientated and showing less than 0.3° short wavelength misorientations (Fig. 10c and Fig. S5). This misorientation angle is comparable to the accuracy of the EBSD measurements performed with the Crystal Probe. However, as the small elongated subgrains coincide with the healed short microfractures or the alignments of tiny fluid inclusions (arrows on Fig. 10a and 10b), they are believed to be significant even if their misorientation is very small (<0.2°, see Fig. S5). Misorientation axes corresponding to some of these subgrains have been determined (Fig. 10d) and are close to [01-11] or [01-12].

The same area has been then analyzed by X-ray Laue microdiffraction. A high definition map with a 2.5 µm step (89 lines, 101 columns, 8989 images) was constructed on the 250 x 220 μm^2 zone. In this area, the relative simplicity of the Laue images (low number of subgrains within the analyzed volume) allows measuring the orientation and local deviatoric distorsion of the quartz unit cell with a good precision (~0.1 mrad). The crystallographic orientation was determined in each point of the map and the rotations Rx, Ry and Rz of the crystal lattice around the x, y and z axes (sample referential, see Fig. 2) relative to the average orientation matrix were calculated (Fig. 11a ; see Appendix A1 for the details of calculation and methods of data filtering).

The spatial and angular resolutions obtained with X-ray Laue microdiffraction are lower and higher, respectively, than those obtained with EBSD. However, these two techniques sample different regions as EBSD samples the surface and X-ray Laue microdiffraction a volume of 1 x 1 x 100 μm^3, respectively (see Analytical Procedures). There is a good correlation between the domains indicated by Rx , Ry and Rz rotations calculated with Laue Tools Package applied on X-ray Laue microdiffraction data (Fig. 11a) and on EBSD data (Fig. 11b). The subgrain boundaries correspond to the misorientation

IST 26/1/18 12:12
Supprimé: -

IST 12/1/18 11:52
Supprimé: s

IST 12/1/18 14:50
Supprimé: with the same order of

IST 12/1/18 14:51
Supprimé: as

IST 12/1/18 14:51
Supprimé: se

IST 15/1/18 10:25
Supprimé:

IST 12/1/18 14:53
Supprimé:

maps and the misorientation angles measured with the two methods are comparable (Fig. 11a and 11b). These maps also indicate that Ry misorientations are larger than Rz and Rx for both techniques. Moreover, the Ry map highlights the small-elongated subgrains parallel to the healed short microfractures or the alignments of tiny fluid inclusions.

6.2 Lattice distorsion - Elastic strain

The deviatoric elastic strain measurement performed by X-ray microdiffraction is based on the slight distorsion of the measured Laue pattern compared to the pattern of an undeformed crystal of the same orientation, *i.e.,* the angular distances between spots of the Laue patterns in the deformed crystal are compared to those of an undeformed reference pattern. The data have been filtered using two estimators of the quality of the Laue pattern refinement (number of spots and average distance between experimental and reference pattern spots, see Appendix A1 for explanation). It is possible to calculate the six main components of the deviatoric elastic strain tensor (ε_{XX}, ε_{YY}, ε_{ZZ}, ε_{YZ}, ε_{XZ}, ε_{XY} with $\varepsilon_{XX} + \varepsilon_{YY} + \varepsilon_{ZZ} = 0$) on each point of the map (Fig. S6). Values of equivalent strain may be calculated from the strain tensor :

$$\varepsilon_{eq} = 2/3\ [(\varepsilon_{XX} - \varepsilon_{YY})^2 + (\varepsilon_{YY} - \varepsilon_{ZZ})^2 + (\varepsilon_{ZZ} - \varepsilon_{XX})^2 + 6\ (\varepsilon_{XY}^2 + \varepsilon_{XZ}^2 + \varepsilon_{YZ}^2)]^{1/2} \qquad (1)$$

and are reported without filtering (Fig. 12a) or after filtering (Fig. 12b). Equivalent strain and the components of the elastic strain tensor (Fig. S6) are roughly correlated with the microstructures revealed by EBSD (sub-grain boundaries, see Fig. 10b), with the Rx, Ry and Rz maps (Fig. 11), and with microfractures as well. However, some domains with no important misorientation or subgrains such as the upper left corner on the map (Fig. 11), display important elastic strain (more than 2.5 10^{-3}, Fig. 12).

The distribution histograms of the equivalent strain value in each point of the map is given in Fig. 13a. Without filtering equivalent strain varies up to more than 2.5 10^{-3}, but the highest values (>2.5 10^{-3}) removed by filtering. Nevertheless, mean equivalent strain after filtering is still at 0.96 10^{-3}.

6.2 Residual stresses

The distorsion of the crystal lattice measured above is purely elastic, thus the residual deviatoric stress tensor may be calculated on each point of the map by applying the Hooke's law :

$$\sigma_{ij} = C_{ijkl}\ \varepsilon_{kl} \qquad (2)$$

where σ is the stress, ε_{kl} the elastic strain and C_{ijkl} the elastic coefficients for α-quartz as determined by Ogi et al. (2006) at 30°C. Because of the proportionality between elastic strain and stress, the maps representing the components of the residual deviatoric stress tensor are similar to the map of the elastic strain components.

The von Mises (or equivalent) stress is a useful scalar to compare the state of stress at different location in a crystal. As for equivalent strain, the von Mises stress was calculated on each point of the map following the equation :

$$\sigma_{eq} = (1/2\ ((\sigma_{xx}-\sigma_{yy})^2 + (\sigma_{yy}-\sigma_{zz})^2 + (\sigma_{xx}-\sigma_{zz})^2 + 6\ ((\sigma_{yz})^2 + (\sigma_{xz})^2 + (\sigma_{xy})^2)))^{1/2} \qquad (3)$$

IST 5/3/18 12:29
Supprimé: . ... [2]

IST 12/1/18 11:52
Supprimé: Figure…ig. 12a) or after filterir ... [3]

IST 11/1/18 14:53
Supprimé: residual stress…esidual deviato ... [4]

IST 25/1/18 15:20
Supprimé: Thus, the…ecause residual stre ... [5]

IST 11/1/18 15:07
Supprimé: As for equivalent strain, …he ... [6]

and reported as a distribution histogram (Fig. 13b). The distribution of the filtered von Mises stress displays a modal value at 100 MPa for a mean at 141 MPa.

As pointed out by the anonymous referee, the deviatoric stress and von Mises stress obtained from deviatoric strain measurements are only approximate due to the trigonal structure of the quartz which creates coupling between deviatoric strain (stress), and expansion stress (strain, respectively). The largest error due to this approximation is 24 MPa (see SM7 for an evaluation of the error). For simplicity, the term "Von Mises stress" is used in this paper as a shortcut for "pseudo Von Mises stress calculated from deviatoric strain".

7 Interpretation and discussion

The NOJ220 sample studied in this paper is located at 51.3 m from the main Nojima fault, that is outside the damage fault zone determined on the basis of studies of the drillcore samples (Ohtani et al., 2000a; Tanaka et al., 2001). Deformation microstructures corresponding to a low strain are nevertheless present in the thin section. We discuss now the observed microstructures in terms of stress and strain-rate, *i.e.* their time of formation in relation with a seismic rupture (Fig. 14), and their significance in the development of the damage zone around the Nojima fault.

7.1 Laumontite-filled veins

Two types of veins or microfractures have been defined in the NOJ220 sample. The fact that all of them are sealed by laumontite clearly indicates that they accompanied the first period of seismic activity on the Nojima fault (Boullier et al., 2004a) around 56 Ma (Murakami and Tagami, 2004). As already pointed out, the laumontite stability field in the 100-300 MPa pressure range (Cho et al., 1987) constrains the depth of formation of these veins at 3.7-11.1 km depth. The E-W orientation of the two types of laumontite veins is not consistent with the left-lateral wrenching kinematics of the Nojima fault during its first period of activity. This point will be discussed later.

What could we say on the kinetics of opening and sealing of these veins and microfractures ? In the E-W striking breccia-like veins, the large and angular fragments of minerals suggest the absence of attrition. The fragments were transported away from their source locality by fluid advection in the fractures at least before the complete sealing by laumontite. Thus, the opening of one breccia-like vein corresponds to a single transient high permeability stage in the Nojima fault vicinity and is interpreted to have occurred during a single seismic event. Fracture opening has induced post-seismic circulation of a hot fluid coming from greater depths and crystallizing laumontite during cooling (Fig. 14). Two breccia-like veins are observed in the studied thin section. Either these two veins were formed during the same seismic event, either they were formed during two different but similar earthquakes.

The significance of the second type of veins is not so clear. The morphology of the laumontite prisms and their orientation with respect to the vein walls confirm that they are mode I opening fractures and suggest equal rates of vein opening and laumontite growth by comparison with numerical modelling of vein opening and sealing (Hilgers et al., 2001). These veins

IST 11/1/18 11:07
Supprimé: peak

IST 12/1/18 15:07
Supprimé: The

IST 8/3/18 16:27
Supprimé: and indicate that the veins were formed in a single event of dynamic fracturing (Fig. 14)

IST 26/1/18 11:43
Supprimé: s

IST 8/3/18 16:32
Supprimé: ,

IST 8/3/18 16:32
Supprimé: by comparison with numerical modelling of vein opening and sealing (Hilgers et al., 2001)

are E-W orientated and on average parallel to (or branched on) the breccia-like laumontite-filled veins and thus are probably associated to them. However, they do not contain mineral fragments; this may be due either to their smaller thickness preventing the transport of fragments by the advecting fluid or to a slower rate of fracture opening. The type 2 veins and especially the dense array illustrated in Fig. 6, are also very similar in shape to the experimental fractures described by Aben et al. (2016). These authors have performed successive high strain-rate loadings (180 s^{-1} to 90 s^{-1}) on granitic cylinders using Hopkinson bars below the pulverization threshold in order to simulate successive seismic events. The numerous fractures created in these experiments run roughly parallel to the loading direction and show only dilation and no shear (Aben et al., 2016). The quartz grain described in the Fig. 7 and displaying fractures radiating in a Hertzian pattern may also be compared to quartz grains in damaged sandstones along the San Andreas Fault (Dor et al., 2009). By analogy, the opening of type 2 laumontite veins is tentatively attributed to co-seismic or dynamic stage (Fig. 14) although their orientation is more difficult to interpret (E-W striking veins versus N50° striking Nojima fault). Do these veins represent one or several seismic events? Following Aben et al. (2016) additional loading led to the growth of new fractures rather than failure on the already created fractures resulting into homogeneously distributed fractures within the sample. Therefore, the sum of the veins either breccia-like or mode I that are observed in the NOJ220 sample may correspond either to several similar « mild » seismic events characterized by similar loading conditions (characteristic earthquakes) or to the propagation of a single seismic rupture. If a single event is favoured for the formation of the fracture array shown in Fig. 6, it is probable that all the laumontite veins observed in the thin section formed during several similar earthquakes. Whatever the interpretation, the consequence of coseismic fracturation is a fast and transient increase of the permeability allowing circulation of hot advecting fluids and sealing of fractures by laumontite (Fig. 14).

IST 8/3/18 16:33
Supprimé: on average

IST 10/1/18 15:03
Supprimé: ,

IST 26/1/18 11:46
Supprimé: a

IST 26/1/18 11:52
Supprimé: The second interpretation is favoured because no clear cross-cutting are observed, but branching relationships between veins were observed.

7.2 Microfractures and alignments of tiny fluid inclusions in quartz

What are the relationships between the formation of microfractures and of the alignments of tiny fluid inclusions? As described above, the alignments of tiny fluid inclusions are well orientated at the sample scale (Fig. S1), independently of the orientation of the host quartz crystal and are parallel to the Nojima fault. Therefore, we may infer that quartz behaves as an isotropic material during the dispersion of large fluid inclusions into tiny ones and that this phenomenom is related to the macroscopic tectonic loading. Small intragranular microfractures and alignments of tiny fluid inclusions have the same cathodoluminescence signatures (Fig. S2 and S3), identical to that of quartz in the vicinity of laumontite-filled veins. Consequently, both microstructures are spatially linked and are interpreted to have formed simultaneously at a geological time scale. The alignments of tiny fluid inclusions are associated with a small (<0.3°) lattice misorientation visible on the EBSD map in Fig. 10b indicating that they result from a combination of brittle and plastic deformation of the quartz lattice. By comparison with experimental studies where fluid inclusion-rich quartz are submitted to a 10^{-8} to 5.10^{-9} strain-rate under 200-600 MPa at 200-800°C in a Griggs apparatus (Tarantola et al., 2010) and with similar natural fluid inclusions (Diamond and Tarantola, 2015), alignments of tiny fluid inclusions are tentatively interpreted as decrepitated large former fluid inclusions in an anisotropic stress regime. They are perpendicular to the principal stress in experiments (Tarantola et al.,

IST 11/1/18 11:41
Supprimé:

IST 11/1/18 11:39
Supprimé: Pêcher, 1981;

2010) or to the regional compression in natural samples (Diamond and Tarantola, 2015). Recent similar experiments have confirmed this observation (Stünitz et al., 2017).

Decrepitation or dispersion of the former large fluid inclusions was probably accompanied by contamination of the primary fluid in the inclusion by the laumontite-bearing fluid circulating in microfractures during the first period of seismic activity of the Nojima fault. Decrepitation was then followed by a stress-driven dissolution-diffusion-precipitation mechanism leading to fracture healing and formation of neonate fluid inclusions. It is believed that decrepitation of large fluid inclusions and microfracturing occurred during the seismic stage, and that healing of alignments of tiny fluid inclusions took place during the post-seismic stage. If healing is a slow mechanism at the experimental time-scale (several days or weeks; Pêcher, 1981; Brantley, 1992 ; Tarantola et al., 2010), it may contribute to the relatively fast post-seismic strengthening and seismic velocity recovery observed along active faults during a few months after an earthquake (Brenguier et al., 2008).

In their experiments, Tarantola et al. (2010) and Stünitz et al. (2017) have demonstrated that alignments of tiny fluid inclusions form in a plane perpendicular to the maximum compressive stress. Even more, the direction of the alignments of tiny fluid inclusions in the NOJ220 sample is roughly parallel to kink-bands in biotite (Fig. S1), which themselves form perpendicular to the maximum compressive stress (Cummings, 1965). This suggests that maximum compressive stress was at high angle to the Nojima fault in the crust when the alignments of tiny fluid inclusions and kinks in biotite formed. This configuration of stress is consistent with that measured by Ikeda et al. (2001) 1.5 years only after the Kobe earthquake and characterized by the maximum stress being perpendicular to the Nojima fault trace as near the San Andreas fault at Cajon Pass, California (Shamir and Zoback, 1992).

7.3 Plastic deformation of quartz

Deformation microstructures observed in quartz in the NOJ220 sample give informations on stress and strain-rate. The maps of crystallographic orientation of quartz in the NOJ220 sample show Dauphiné twins and misorientation domains or subgrains that are indicative of a plastic deformation. The cross-cutting relationships between subgrain boundaries indicate that the large subgrains formed before the small ones and may be attributed to the cooling history of the granodiorite as frequently observed in granitic rocks (Nédélec and Bouchez, 2011). Sub-grain size is related to stress during plastic deformation (Sherby et al., 1977) by the equation $\lambda=Ab(\sigma/E)^{-1}$, where λ is the sub-grain size, A is a dimensionless constant of proportionality which is approximately equal to 4 for many materials, b is the Burgers vector length, σ is stress, and E is Young's modulus. Therefore, a regime of increasing stress would result in reducing sub-grain sizes nested in larger sub-grains during plastic deformation as observed in the NOJ220 sample. Small subgrains or short wavelength misorientations are classically observed in rocks naturally deformed at low temperature (see for example Derez et al., 2015) or experimentally deformed at high temperature but high stress and strain-rates (Trepmann, 2009; Trepmann and Stöckert, 2013; Trepmann et al., 2017). The small subgrains are elongated parallel to the microfractures and alignments of tiny fluid inclusions suggesting that the three types of microstructures are issued from the same high stress deformation event.

IST 12/1/18 15:15
Supprimé: and characterizing

IST 10/1/18 15:05
Supprimé: Actually

IST 8/3/18 16:46
Supprimé: t

IST 23/1/18 16:14
Supprimé: Alteratively as s

IST 23/1/18 16:14
Supprimé: ,

IST 8/3/18 17:29
Supprimé: The small subgrains are elongated parallel to the microfractures and alignments of tiny fluid inclusions suggesting that the three types of microstructures are issued from the same deformation eventevent.

IST 11/1/18 15:51
Supprimé: If s

IST 26/1/18 12:12
Supprimé: -

IST 11/1/18 15:52
Supprimé: described

IST 12/1/18 15:24
Supprimé:

Misorientation axes of the small subgrains have been determined in the quartz grain mapped using EBSD and were identified as [0001] (Fig. 5 and 8) but were close to [01-11] or [01-12] in the small area mapped with a high resolution (Fig. 10). They could give information on the active glide systems and on deformation conditions provided that their orientation and nature (tilt or twist boundary) are known (Lloyd, 2004). Unfortunately, we did not perform TEM observations to determine dislocation microstructures in the NOJ220 sample. However, more important than the activated glide systems are the small size of the elongated subgrains, the absence of bulging at grain boundaries, and the presence of microfractures that are all together characteristic of a deformation occurring in the semi-brittle faulting regime of quartz as defined by Hirth and Tullis (1994) and Tullis (2002) on the basis of experiments at high strain-rate and low temperature ($>10^{-6}$ s^{-1}, <700°C). Extrapolation of experimental results to natural conditions (T < 300° C as shown by the presence of laumontite) indicates a strain-rate higher than 10^{-5} s^{-1} (Tullis, 2002). The absence of recrystallization, the small angle of misorientation (<5°) and the 5% maximum shortening of biotite cleavages indicate a low finite strain. High strain-rate and low strain combined together suggest that microstructures originated during a short duration transient deformation event such as a seismic rupture.

Because of the emergence of new techniques to measure complete crystallographic orientation of quartz, Dauphiné twinning is now recognized in naturally deformed quartz-bearing rocks. Dauphiné twins may form in nature in a wide range of strain-rate conditions from mylonitic quartzites (Lloyd, 2000, 2004 ; Pehl and Wenk, 2005 ; Menegon et al., 2011) to meteoritic impact (Wenk et al., 2005, 2011). Experimental studies were performed to investigate the influence of stress and temperature on Dauphiné twinning and have shown that it initiates at 50-100 MPa at 500°C and that activation twinning is temperature dependent (Wenk et al., 2006). Recently, Wenk et al. (2011) have described Dauphiné twins in quartz from shock experiments, impact structures, pseudotachylites and fault breccias, and conclude that these microstructures are diagnostic of high and transient seismic stresses. Thus, Dauphiné twins observed in quartz from the NOJ220 sample are tentatively attributed to one or possibly several episodes of high and transient seismic stresses. Twinning immediately preceded microfracturing and fragmentation as shown by cross-cuting relationships and their continuity in neighbouring fragments in Fig. 5, 8, 9 and 10. Therefore, they are suggested to have formed during the rising stress time before the seismic rupture (Fig. 14).

7.4 Elastic strain and residual stress

Elastic strain in a quartz grain was measured with X-ray Laue microdiffraction, which allowed the calculation of the associated residual stress. What could be the origin of the residual stresses measured in quartz? How such large residual stresses may be preserved in a small volume for such a long time? One could argue that the residence of the sample at depth, i.e., under confinement, could have preserved the residual stresses in the quartz grains. In this case, these residual stresses should have been released during recovery by drilling and during sawing and thinning for thin section manufacturing. Therefore, confinement at depth is not a sufficient condition for preserving residual stresses. As discussed above, the studied quartz display torsions and flexions of the quartz lattice, and subgrains or dislocation walls, which are attributed to

IST 12/1/18 15:32
Supprimé: for quartz

IST 12/1/18 15:31
Supprimé: two areas

IST 12/1/18 11:53
Supprimé: s

IST 12/1/18 15:33
Supprimé: or

IST 8/3/18 17:20
Supprimé: T

IST 8/3/18 17:21
Supprimé: as a sealing mineral of microfractures

IST 8/3/18 17:21
Supprimé: a temperature in the range for this regime (<300°C) and, by extrapolation of experimental results to natural conditions

IST 8/3/18 17:32
Supprimé: and

IST 8/3/18 17:34
Supprimé: , less than 5% as shown by the maximum shortening measured with (001) cleavages in biotites.

IST 12/1/18 11:53
Supprimé: s

IST 5/2/18 10:00
Supprimé: such

IST 5/2/18 10:02
Supprimé: The fact that residual stresses are measured in a small volume of the thin section suggests that confinement at depth is not the cause of their persistence during long periods of time otherwise they should be released by thin section processing and we should not be able to measure them.

dislocation creep under low temperature and high transient stress or strain-rate as quoted above. It is known that a local stress field is associated to each dislocation or dislocation wall because they correspond to a local elastic distorsion of the crystallographic framework (Dieter, 1976 ; Nicolas and Poirier, 1976). Thus, we tentatively interpret the measured residual stresses as the sum of the local stresses attached to each dislocation or dislocation wall present in the quartz grain.

The maps of elastic strain indicate that the ε_{ZZ} component is slightly lower than the others. This could be interpreted as partially released elastic strain close to the free surface of the sample as suggested by Chen et al. (2015), who obtain the same results for a deformed quartz grain in the San Andreas fault zone. However, as the studied NOJ220 thin section is horizontal, such lower ε_{ZZ} strain component could be also related to the strike-slip tectonic environment of the Nojima fault during the Paleocene (Famin et al., 2014) corresponding to a vertical minimum compressive stress at that geological time. Supplementary X-ray microdiffraction studies on differently orientated thin sections are necessary to test these different interpretations.

The large gradients in elastic strain (xx, yy and zz, yz, xz and xy, Fig. S6) are roughly matching the microstructures (subgrain boundaries or microfractures). They correspond well to the threshold values of the two quality estimators and to the minimum values of diffracted intensity (see Appendix A1, Fig. A1). Thus, high elastic strain or distorsion of the lattice may prevent a good fitting of the spot positions in the Laue pattern (the single-unit-cell model used to describe the pattern starts to fail). Nevertheless, after filtering these points out, the mean value of von Mises stress remains high (141 MPa versus 223 MPa if not filtered) in the small 250 x 220 μm^2 studied area included in a single quartz grain (Fig. 13b).

We have only performed one scan in the NOJ220 sample using X ray microdiffraction and the representativity of this scan may be questionned. All quartz grains present in the NOJ220 sample display microstructures similar in style and intensity (microfracturing, dispersed fluid inclusions, short wave length misorientation, …) except along the array of very dense microfractures (Fig. 6 and 7) where these microstructures are more intense. Therefore, we believe that the residual stresses measured in such a small studied domain are representative of the whole sample and may represent a lower bound compared to the microfracture array quoted above.

Chen et al. (2015) obtained 130 MPa as a modal value in the histogram of von Mises stresses in a cataclastic quartz sample located 50 m away from the San Andreas Fault active zone in the SAFOD drillhole (California), and 200 MPa in a quartz located within the Vredefort meteoritic impact site in South Africa. Lower values (*ca* 50 MPa) are obtained by Kunz et al. (2009) in the mylonitic (*i.e.* plastically deformed) Santa Rosa granite (California). Thus, our results (modal value in the histogram of von Mises stresses at 100 MPa) compare well to the values published by Chen et al. (2015) for quartz samples of the San Andreas fault zone although the NOJ220 studied sample is located outside of the damage zone of the Nojima fault.

As pointed out by Chen et al. (2015) the residual stresses have remained in the crystals for very long time, as long as 2 b.y. in the case of the Vredefort impact. In the Nojima fault sample, elastic strain and residual stress have been preserved since 56 Ma, age of the first period of seismic activity of the fault (Murakami and Tagami, 2004). They were not released during the uplift of the area from 3.7-11.1 km depth (depth range of laumontite stability) to the near surface (<1 km depth), or

IST 12/1/18 15:40
Supprimé:), and

IST 12/1/18 15:40
Supprimé: t

IST 12/1/18 11:53
Supprimé: s

IST 24/1/18 12:27
Supprimé:

IST 12/1/18 15:41
Supprimé: think it is possible

IST 11/1/18 11:08
Supprimé: peak

IST 11/1/18 11:08
Supprimé: peak

IST 10/1/18 16:47
Supprimé: , mean at 141 MPa

IST 12/1/18 15:43
Supprimé: and

during the Quaternary phase of seismic activity of the Nojima fault since 1.2 Ma. We believe that, in the present case, internal stresses could not be released after dynamic damage due to the very low temperature (<300°C) inhibiting reorganization of entangled dislocations and recrystallization of quartz, the later being a potential marker of stress relaxation (Trepmann et al., 2017).

7.5 Implications for the development of the damage zone

As discussed above, we interpret the laumontite-filled veins, the microfractures and fluid inclusion decrepitation as resulting from co-seismic fracturing during characteristic earthquakes on the Nojima fault and the Dauphiné twinning and plastic deformation of quartz as high strain-rate precursors of these dynamic events. These earthquakes left behind high von Mises stresses in the sample (modal value at 100 MPa, mean at 141 MPa). Earthquakes characterizing the first period of seismic activity along the Nojima fault were M6 to M7 magnitude events (Boullier et al., 2001). Their consequences may be compared to those of Californian earthquakes along the San Andreas fault system where pulverized rocks were produced on the near surface within a 100 m wide zone (Dor et al., 2006 ; Rockwell et al., 2009). We believe that microstructures in the NOJ220 sample are representative of the incipient dynamic damage at depth induced by the propagation of seismic ruptures on the Nojima fault plane 51 m away from the studied sample. Imprints of this damage are resumed to a few fractures which are now sealed within laumontite, and to residual stresses and microscale deformation structures in quartz. We postulate that successive seismic ruptures would cumulate residual stresses until exceeding the strength of the rock. While the strength of the undeformed and unaltered protolith of the Nojima fault is around 400 MPa at an effective confining pressure of 50 MPa, samples located at 14.5 m and 5 m from the fault plane have a 200 MPa and 150 MPa strength, respectively (Lockner et al., 2009). Thus, the residual stresses accumulated in the studied NOJ220 sample are already close to that of the damaged granodiorite and could have contributed to the softening of the fault wall and widening of the observed 45m wide damage zone (Ohtani et al., 2000a ; Tanaka et al., 2001).

As pointed already, microstructures in the NOJ220 sample are very similar to the experimentally or naturally fragmented samples described by Aben et al. (2016), Dor et al. (2006, 2009), and Rockwell et al. (2009). We know that high confining pressure prevents complete pulverization but not fragmentation (Yuan et al., 2011). The confining pressure being in the 100 - 300 MPa range when microstructures formed in the NOJ220 sample, the strain-rate threshold was probably not attained and the granodiorite was microfractured, but not pulverized. The high stresses associated with the propagating seismic waves have induced elastic strain which has not been completely released by the microfracturing process as shown by the matching with high elastic strain gradients and microfractures (Fig. S6). X-ray microdiffraction allows today to measure the residual stresses remaining in the sample.

In their experiments, Aben et al. (2016) have shown that the pulverization threshold can be reduced by successive dynamic loadings at lower strain-rate if the rock experiences dynamic fracturing during successive loadings. They show that each dynamic event leads to the growth of additional microfractures homogeneously distributed and that P-wave velocity decreases with an increasing amount of damage. P and S-wave velocities have been measured on the GSJ Hirabayashi

IST 24/1/18 14:05
Supprimé: a

IST 24/1/18 14:05
Supprimé: ration

IST 26/1/18 12:00
Supprimé: a

IST 26/1/18 11:58
Supprimé: same

IST 24/1/18 14:06
Supprimé: that

IST 11/1/18 11:08
Supprimé: peak

IST 24/1/18 14:07
Supprimé: and

IST 24/1/18 14:07
Supprimé: t

IST 24/1/18 14:06
Supprimé: californian

IST 26/1/18 12:00
Supprimé: a

IST 9/3/18 10:34
Supprimé: enlargment

IST 10/1/18 15:07
Supprimé: and

IST 24/1/18 14:09
Supprimé: repectively

IST 24/1/18 14:44
Supprimé: ,

IST 24/1/18 14:45
Supprimé: , and which could be measured today by

drillcore samples by Zamora et al. (2000). At 204m depth (d_{fault} = 53.2 m) mean V_P is 5320 m.s^{-1} on dry samples but falls at 4950 m.s^{-1} at 220m depth (d_{fault} = 51.3 m) in the same core piece as the sample studied in this paper. Such a 7% decrease in V_P velocity is another indicator for unvisible damage in the sample whatever the dynamic or quasi-static origin of the damage. An important difference between experiments and natural fault zones is that fluid circulates during the interseismic period. Post-seismic hydrothermal healing of the dynamically created microfractures partially increases the strength of rocks as laumontite does in the Nojima samples (Fig. 14). Nevertheless, high residual stresses measured today by X-ray Laue microdiffraction may be considered as a record of the propagating seismic waves along the Nojima fault.

As pointed out earlier, the E-W orientated mode I laumontite veins are not consistent with the far-field tectonic setting of the fault, i.e. left-lateral wrench fault with N-S compression (Famin et al., 2014). If all the steps in the process of orienting the core sample and thin section are correct, these fractures do not correspond to quasi-static loading conditions. Only dynamic loading may explain them as induced by a sudden release of the accumulated tectonic compressive stresses. The elastic energy released by this way may trigger extensional fractures and overshoot (Savage and Wood, 1991).

7.6 Implications on the dynamic damage mechanism

All the deformations described in this paper are interpreted as dynamically induced at a 51.3m distance away from the Nojima fault. Do these observations provide information on the loading mechanism at the origin of the dynamic damage? Several processes have been recently proposed in the literature for explaining shallow damage zone pulverization (see review in Aben et al., 2017): dynamic compressive loading, dynamic tensile loading, fluid-assisted decompression, wrinkle-like pulses and super-shear.

Experiments reproducing compressive loading using Split-Hopkinson bars have produced microstructures qualitatively similar to those observed in the described sample. Thus, as suggested in this paper, compressive loading may be a good candidate for the dynamic damage on the Nojima fault. Experiments reproducing tensile loading are more difficult to realize (see review in Zhang and Zhao, 2013) and require specific sample shapes. These experiments reproduce simple fractures rather than pulverization (Zhang and Zhao, 2013). No microstructural analyses are available for comparing with the microstructures in the Nojima sample. Nevertheless, one has to keep in mind that dynamic tensile strength is lower than dynamic compressive strength (Zhang and Zhao, 2013) and that dynamic tensile loading should be easier to produce than dynamic compressive loading.

The fluid-assisted decompression model corresponds to hydro-fracturing due to a sudden drop of fluid pressure in the rock. If this mechanism may be efficient in high permeability sedimentary rocks present in the subsurface, it appears highly improbable in the case of the Nojima granodiorite, which has a very low permeability (10^{-8} to 10^{-9} darcy under 50MPa confining pressure, Lockner et al., 2009).

Considering the model of wrinkle-like pulses related to a bimaterial interface (Shi and Ben-Zion, 2006), it is not appropriate in the present case because both foot-wall and hanging-wall of the Nojima fault are constituted by the same granodiorite and the profile of physical properties of rocks across the fault is symmetrical (Lockner et al., 2009). Moreover, this model does

IST 10/1/18 16:49
Supprimé: dynamic

IST 9/3/18 10:38
Supprimé: ing

not apply at great depth (> 3 km, Ben-Zion and Shi, 2005) where dynamic damage has been demonstrated to occur in the Nojima sample on the basis of laumontite in veins and microfractures.

The last model is the supershear, i.e., a rupture front propagating faster than the S-wave velocity (Bouchon et al., 2001) and the formation of a Mach-cone (Rosakis et al., 2007). If supershear is mostly observed during high magnitude earthquakes along simple large faults (Bouchon and Vallée, 2003), it may also occur along smaller linear segments (see review in Rosakis et al., 2007). It triggers damage laterally and also in depth (Bouchon and Karabulut, 2008). Thus, supershear could be invoked for inducing the dynamic damage at 51.3 m from the Nojima fault and at 3.7 - 11.1 km depth.

To conclude, microstructures observed in the unique sample studied in this paper are interpreted as due to dynamic damage. However, suggesting a unique mechanism for explaining this dynamic damage would be over-interpretating the data. Additional microstructural observations are necessary on orientated samples across the Nojima fault, including samples outside and inside the damage zone.

8 Conclusions

We have studied a core sample of granodiorite located at 51.3 m from the Nojima fault (Japan) that was drilled after the Hyogo-ken Nanbu (Kobe) earthquake using EBSD and high resolution X-ray Laue microdiffraction. Although macroscopically undeformed, the sample is pervasively microfractured and locally fragmented during the first stage of seismic activity along the Nojima fault. On the basis of the sealing hydrothermal laumontite, we are able to estimate that microfracturing occurred at 100-300 MPa confining pressure, *i.e.* at 3.7 – 11.1 km depth. EBSD mapping was used to characterize the crystallographic orientations and deformation microstructures in the sample, and X-ray Laue microdiffraction to measure elastic strain tensor in a quartz grain. Both methods give consistent results on the crystallographic orientation and show small and short wavelength misorientations associated with laumontite-sealed microfractures and alignments of tiny fluid inclusions. Deformation microstructures are symptomatic of the semi-brittle faulting regime in which low temperature brittle and plastic deformation and stress-driven dissolution-precipitation processes occur conjointly.

Using the Hooke's law, residual stresses and von Mises stresses are calculated from residual elastic strain measured by X-ray Laue microdiffraction. The von Mises stress distribution shows a modal value at 100 MPa, a value similar to that obtained on quartz located at 50 m from to the San Andreas fault gouge. Such stress values are comparable to the peak strength of a damaged granodiorite from the damage zone around the Nojima fault indicating that, although apparently macroscopically undeformed, the sample is actually significantly damaged. The homogeneously distributed microfracturing of quartz is the microscopically visible imprint of this damage and suggests that high stresses were stored in the whole sample and not only concentrated on some crystal defects. It is proposed that the high residual stresses are the sum of the stress fields associated with dislocations and dislocation microstructures that were triggered by the dynamic damage related to the propagation of rupture fronts or seismic waves associated to M6 to M7 earthquakes during Paleocene on the Nojima

IST 24/1/18 16:10
Supprimé: .

IST 5/2/18 10:24
Supprimé: and residual stresses

IST 26/1/18 12:12
Supprimé: -

IST 10/1/18 15:08
Supprimé: deposition

IST 10/1/18 16:53
Supprimé: and

IST 11/1/18 11:08
Supprimé: peaks

IST 10/1/18 16:53
Supprimé: (mean 141 MPa)

fault at a 3.7 – 11.1 km depth where the *in situ* confining pressure prevented pulverization. The high residual stresses and the deformation microstructures would have contributed to the widening of the fault zone with additional large earthquakes occurring on the Nojima fault.

IST 9/3/18 10:46
Supprimé: enlargment or

9 Appendix A1 - X-ray Laue microdiffraction : method and parameters for the analysis of the series of Laue patterns

The methods for sample alignment and geometry calibration using the Laue pattern of a Ge single crystal were described in Ulrich et al. (2011). The three main stages of automated analysis of a Laue pattern (peak search, indexation, unit cell dimensions and orientation refinement) were described in Tamura (2014) and Robach et al. (2017), and also in the documentation of the LaueTools software.

For the quartz sample studied here, as described in Fig. 2c, two types of Laue patterns are encountered : type 1 : single-crystal (one spot per HKL) Laue patterns, (about 70% of the map) and type M : multiple closely-oriented subgrains (several sub-spots per HKL) Laue patterns (about 30% of the map). For type 1 points, the orientation and strain results are essentially "single-valued", *i.e.* are reproducible over a wide range of analysis parameters.

For type M points, a criterion needs to be arbitrarily chosen in order to decide which is "the" x,y position of a multi-spot or an asymmetrical spot. Indeed, although in theory a multi-grain indexation procedure could be applied to the multi-spot Laue pattern, in order to individually index each sub-spot present on the beam path, in practice the corresponding code for closely-spaced sub-spots is still unavailable. And at the stage of the display of the 2D maps of strain or orientation, a decision needs to be taken in any case, in order to select the individual sub-grain or the mean grain to be displayed at each point. For type M points, results therefore widely vary depending on analysis parameters such as i) the box size for the 2D Gaussian fitting of the spots in the Peak Search stage, ii) the angular tolerance for linking theoretical (undeformed reference crystal) and experimental spots at the SpotLink stage of the Indexation stage, and iii) the threshold on pixel deviation for removing bad spots at the refinement stage.

In addition, there is a limit to the "indexability" of M points : when the groups of sub-spots are too wide, neighbouring groups of sub-spots belonging to different HKL's start to intersect, and the number of indexed spots falls. For a type 1 point, the typical minimum distance between experimental spots is 17 pixels. This sets an upper limit on the width (in pixels) of the groups of sub-spots, above which the brute-force spot-linking process based on pixel-distance only starts to produce ambiguous results (e.g. double-indexed experimental spots or double-linked theoretical spots).

An arbitrary choice was therefore needed for the analysis of the M points. Different indexation strategies were envisaged: a first approach is to try to select the sub-grain closest to the surface, either by selecting the most intense sub-spot in each group (based on maximum pixel intensity, or maximum integrated intensity), or by spot-linking directly on the local orientation matrix determined with EBSD, taking advantage of the near surface-sensitivity of EBSD. Assuming that the angular accuracy of classical EBSD is around 0.3 degrees (5.2 mrad), the EBSD-approach would only work if the sub-spots

in each group were distant by more than 5 pixels. A second approach, the one choosen in this paper, is to average over all the sub-spots of the M point to create an "average sub-grain".

9.1 « One-spot » analysis

Figure A1 illustrates the variations in the orientation maps produced by a change in the criterion used to calculate the x,y position of the experimental multi-spot (M point). Here a box of 201x201 pixels around the position x_pix,y_pix = (1484,1213) (0-222 spot of Fig. 2b) was extracted from the patterns. The positions xy_max and xy_fit of the spot were calculated by taking, for xy_max, the (integer) pixel position of the maximum of intensity, and for xy_fit, the (real) center position of the 1D Gaussian obtained by fitting the intensity profile projected onto the y axis (respectively the x axis) for the x position (respectively the y position). The positions xy_max and xy_fit are mapped in Fig. A1a and A1b respectively. This very simple "one-spot" analysis already allows visualizing the sub-grain structure inside the mapped region. Indeed, as a first approximation, the x (respectively y) position of the spot provides the crystal orientation in rotation around the y axis (Ry) (respectively Rx).

For M points, the choice of xy_max approximately selects the sub-grain closest to the surface, assuming that its crystalline quality remains sufficient to always dominate with respect to deeper sub-grains. The choice of xy_fit corresponds to building an "average grain" at each map point, with a diffraction-wise averaging, *i.e.* giving a larger weight to well-crystallized region, performed over the different sub-grains present on the beam path.

The most remarkable difference between the (a) and (b) maps in Fig. A1 is the sharper aspect of the sub-grain edges in (a). The averaging over depth in (b) therefore leads, as expected, to a degraded lateral resolution, especially when crossing non-vertical sub-grain boundaries (with respect to the thin section). When comparing the sub-grain structure between Fig. A1 and the EBSD misorientation maps of Fig. 11b, a closer similarity with (a) is observed, as expected for a criterion attempting to select the sub-grain closest to the surface at each point.

9.2 « N-spots » analysis

For the N-spots analysis of the Laue patterns, the xy_fit criterion was used (average sub-grain for type M points). The sub-grain edges in the final micro-Laue strain and orientation maps are therefore less sharp than in the EBSD maps.

Since the region mapped with X-rays was inside in a single grain, the analysis of the series of Laue patterns was performed using a "light-weight" two-spots method to obtain the first "guess orientation matrix". Indeed, the "brute force" indexation of a quartz pattern is a CPU-consuming process due to the low symmetry of the crystal and the corresponding large number of possible theoretical angular distances between crystal planes, and a lighter procedure is preferable when processing a large number of images. Here classical indexation was applied to only one pattern, then two widely-spaced low-Miller-index spots were selected : the (0-222) spot (spot 2) already analyzed in Fig. A1, and the (2-203) spot (spot 1) located around xypix = (659,1640). The interest of using low-index spots is that their first neighbor is comparatively far away (147 pixels for spot 2 and 131 pixels for spot 1) : the risk of a spot with a different (HKL) entering the fixed 201x201 pixels-wide

box, due to the rotation of the crystal, is therefore limited. In practice, the highest spot displacement with respect to the box center (using xy_fit) was 147 pixels for spot 2 and 57 pixels for spot 1. After excluding 11 "bad" points (over a total of 9077) the highest displacement for spot 2 was down to 58 pixels.

The two-spot analysis of the series of Laue patterns was performed using the xy_fit positions for the spots. The resulting approximate orientation matrix (with an unstrained unit cell) was then used to perform a spot-link (linking each theoretical spot to its nearest experimental neigbor) with the list of spots resulting from the peak-search procedure. The angular tolerance (between reciprocal lattice vectors) for the spot-linking process was 0.2 degrees.

Three estimators (npeaks, pixdev, and intensity) of the local uncertainty on the shape / orientation of the unit cell, were calculated with the LaueTools software (Fig. A2). The first estimator (npeaks) is the number of Laue spots used for the refinement of the local orientation and the distorted quartz unit cell. For map points with single sharp spots, a low npeaks gives good data quality (npeaks > 15, Fig. A2a). For map points with multiple spots (several subgrains in the beam path), a high npeaks is needed for good data quality (npeaks > 25, Fig. A2), since the position of each "average" HKL spot is less accurate. The second estimator (pixdev, mean pixel deviation, Fig. A2b) is a measure of the fit quality and represents the mean distance between the experimental (as estimated from 2D peak fitting on the detector image) and theoretical (as calculated from the refined orientation and distorted unit cell) x,y pixel positions of the Laue spots, averaged over the npeaks spots of the pattern. One pixel of pixdev typically gives an uncertainty of 10^{-3} $mrad^{-1}$ on the strain / orientation components. The third estimator is the intensity and represents the average intensity of the 10 most intense spots of the Laue pattern of the grain (Fig. A2c). The spot intensity is the height (peak minus background) of the 2D Gaussian used to fit the 2D image in a box of 101 x 101 pixels around the spot center (boxsize = 50). The search for local maxima in the image (which produces the list of x,y pixel positions of spot centers) was performed using the "convolution" method, which proceeds as follows : first the image is convoluted with a 2D mexican hat function with a FWHM of 3 pixels. This attributes all the Laue spots with a similar width. Thresholding is then applied on the convoluted image (thresholdConvolve = 3000), producing a first mask. The intense pixels in this mask are then grouped by clusters (blobs) based on a "+"-like connectivity criterion. The list of clusters is then reduced by applying a criterion of a minimal distance between two clusters (PixelNearRadius = 50 pixels). The list of remaining clusters is then reduced again by thresholding on the non-convoluted image, after subtracting the local background : Iraw - Ibackground > 50 (IntensityThreshold = 50) where Ibackground is the mean intensity on the frame of a box of 101x101 pixels (boxsize = 50) centered on the cluster center. The resulting mask is shown on Fig. A2d.

After the spot-link stage, the orientation and shape of the unit cell (strained orientation matrix) was refined once using the N indexed spots, then the new pixel deviation (pixdev) between experimental and theoretical spots was calculated, and the refinement was run again after excluding spots with a pixdev larger than 3. This leads to the final values for npeaks and pixdev displayed in Fig. A2a and A2b. Figure A2d illustrates the filtering used for the final display of the elastic strain maps of Fig. 12 and S6.

IST 12/1/18 11:57
Supprimé: s

IST 12/1/18 12:03
Supprimé: S5

Finally, we remark that more complete maps (in terms of number of points) can be obtained using only the two-spots analysis. Figure A3 shows the lattice rotation and strain results in this analysis, performed using xy_max instead of xy_fit. Only one scalar strain component is available is this analysis. The strain results obtained using xy_fit are also shown.

10 Appendix A2 - Method used for lifting the ambiguity between Dauphiné twins

For each quartz Laue pattern, two orientations rotated by 180 degrees around c-axis (two Dauphiné twins) are compatible with the positions of the Laue spots. Hence an ambiguity arises in the spot indexation and the orientation matrix. Laue spot intensities need to be analyzed to lift this ambiguity (Chen et al., 2012). As pointed by Dejoie et al. (2011), spots sorted according to theoretical structure factor are usually unsorted with respect to experimental intensities,due to the strong influence of spot energy and theta diffraction angle on experimental intensity. In the case of quartz, both orientations lead to the same spot energy, which simplifies the analysis.

Most of the microLaue map of Fig. 11a is located inside a single twin. In the analysis, the small domain of twinned crystal (visible at the middle-right in the corresponding EBSD map figure 11b) was treated as a domain of normal crystal, so it is invisible in the orientation maps. This domain becomes visible when plotting a map of box intensity (sum of pixel intensities over a box of 200x200 pixels centered on x,y = 659,1640) of spot 2 -2 0 3.

For the dominant twin of the microLaue map, the initial indexation provided by LaueTools was wrong (there was one chance over two, as only the spot positions were used). The ambiguity on the indexation was then lifted in the following manner.

The 196 indexed spots of the pattern were listed with their experimental intensity, the two possible values of the structure factor, the spot energy and 2theta value. Structure factors were calculated using the cctbx web service (https://cci.lbl.gov/cctbx/structure_factors.html) with the following parameters :

- lattice parameters : 4.913 4.913 5.404 90 90 120, space group 152, default convention for space group,
- atom coordinates in asymmetric unit : O 0.408 0.2881 0.23, Si 0.457 0 0.3333.

It was checked that the cctbx-calculated structure factors were consistent in terms of order with the results from the XMAS program of Tamura (2014) : XMAS provides structure factors only indirectly via the possibility of thresholding on the structure factor in the simulated Laue pattern. The spots were then grouped according to both energy and 2theta, and the two structure factors were plotted versus intensity. The comparison between the two curves (normal and twin) showed a better match for the "twin" orientation. More precisely, the spots were grouped by intervals of +/-0.5 keV for the energy and +/-5 degrees for the 2theta, with the intervals centered on the energy and 2theta of an existing spot, starting from the most intense spot. Going up to spot number 67, we obtained 40 cases with at least 2 spots in the group. Over these 40 cases, the twin crystal was favored in 16 cases (monotonous ascending curve for the twin, non "monotonous ascending" curve for the normal), the normal crystal was favored in 3 cases (reverse criterion), and the ambiguity remained in 21 cases.

Author contribution:

AMB performed the microstructural study and participated to EBSD acquisition. OR performed the X-ray Laue microdiffraction data acquisition and processing. FB acquired the EBSD data. BI and DM processed the EBSD data using MTEX. TO and KF provided the sample and the geological knowledge of the GSJ borehole and core samples. All co-authors participated to the interpretation and discussion of results. AMB prepared the manuscript with contributions from all co-authors.

Competing interests:

The authors declare that they have no conflict of interest.

Acknowledgements

The authors thanks M. Bouchon, J. Weiss, M. Montagnat and M.-L. Doan who have greatly contributed to improve a first version of this paper and particularly by discussing the seismological and mechanical implications of our results. Friendly and fruitfull discussions with D. Amitrano and F. Aben on quasi-static and dynamic damage are sincerely acknowledged. The authors thank Olivier Ulrich for assistance with the micro-Laue setup and Jean-Sébastien Micha for help using the LaueTools software. Christophe Nevado is thanked for high quality thin section polishing and Valentina Batanova and Valérie Magnin for their help using SEM cathodoluminescence. The authors are gratefull to Frans Aben and to an anonymous referee. Their comments contributed to greatly improve our paper.

References

Aben, F. M., Doan, M.-L., Mitchell, T. M., Toussaint, R., Reuschlé, T., Fondriest, M., Gratier, J.-P., and Renard, F.: Dynamic fracturing by successive coseismic loadings leads to pulverization in active fault zones., J. Geophys. Res.-Sol. Ea., 121, 2338–2360, 10.1002/2015JB012542, 2016.

Aben, F. M., Doan, M. L., Gratier, J.-P., and Renard, F.: Coseismic damage generation and pulverization in fault zones: Insights from dynamic Split - Hopkinson pressure bar experiments, in: Fault zone dynamic processes: evolution of fault properties during seismic rupture, edited by: Thomas, M. Y., Mitchell, T. M., and Bhat, H. S., Geophysical Monograph, 227, American Geophysical Union, John Wiley & Sons, Inc., 2017.

Amitrano, D., and Schmittbuhl, J.: Fracture roughness and gouge distribution of a granite shear band, J. Geophys. Res.-Sol. Ea., 107, 2375, 10.1029/2002JB001761, 2002.

Austrheim, H., Dunkel, K., Plümper, O., Ildefonse, B., Liu, Y., and Jamtveit, B.: Fragmentation of wall rock garnets during deep crustal earthquakes., Sci. Adv., 3, e1602067, 2017.

Bachmann, F., Hielscher, R., and Schaeben, H.: Texture analysis with MTEX–free and open source software toolbox., Solid State Phenom. 160, 63-68, 10.4028/www.scientific.net/SSP.160.63, 2010.

Ben - Zion, Y., and Shi, Z.: Dynamic rupture on a material interface with spontaneous generation of plastic strain in the bulk, Earth Planet. Sci. Lett., 236, 486–496, 10.1016/j. epsl.2005.03.025, 2005.

Blenkinsop, T. G., and Sibson, R. H.: Aseismic fracturing and cataclasis involving reaction softening within core marerial from the Cajon Pass drill hole, J. Geophys. Res., 97, 5135-5144, 1992.

Bouchon, M.: The state of stress on some faults of the San Andreas system as inferred from near-field strong motion data, J. Geophys. Res., 102, 11731-11744, 1997.

Bouchon, M., Bouin, M. P., Karabulut, H., Toksoz, M. N., Dietrich, M., and J., R. A.: How fast is rupture during an earthquake? New insights from the 1999 Turkey earthquakes, Geophys. Res. Lett., 28, 2723–2726, 2001.

Bouchon, M., and Karabulut, H.: The aftershock signature of supershear earthquakes, Science, 320, 1323-1325, 10.1126/science.1155030, 2008.

Bouchon, M., and Vallée, M.: Observation of long supershear rupture during the magnitude 8.1 Kunlunshan earthquake, Science, 301, 824–826, 10.1126/science.1086832, 2003.

Boullier, A.-M.: Fault zone geology : lessons from drillings through Nojima and Chelungpu faults, in: Geology of the Earthquake Source : A Volume in Honour of Rick Sibson, edited by: Fagereng, A., and Toy, V., Geol. Soc. Spec. Publ., 359, 17-37, 2011.

Boullier, A.-M., Fujimoto, K., Ito, H., Ohtani, T., Keulen, N., Fabbri, O., Amitrano, D., Dubois, M., and Pezard, P.: Structural evolution of the Nojima fault (Awaji Island, Japan) revisited from the GSJ drill hole at Hirabayashi, Earth Planets Space, 56 (12), 1233-1240, 2004a.

Boullier, A.-M., Fujimoto, K., Ohtani, T., Roman-Ross, G., Lewin, E., Ito, H., Pezard, P., and Ildefonse, B.: Textural evidence for recent co-seismic circulation of fluids in the Nojima fault zone, Awaji island, Japan, Tectonophysics, 378, 165-181, 2004b.

Boullier, A.-M., Ohtani, T., Fujimoto, K., Ito, H., and Dubois, M.: Fluid inclusions in pseudotachylytes from the Nojima fault, Japan, J. Geophys. Res.-Sol. Ea., 106, 21965-21977, 2001.

Brantley, S. L.: The effect of fluid chemistry on quartz microcrack lifetimes, Earth Planetary Sc. Lett., 113, 145-156, 1992.

Brenguier, F., Campillo, M., Hadziioannou, C., Shapiro, N. M., Nadeau, R. M., and Larose, E.: Postseismic relaxation along the San Andreas fault at Parkfield from continuous seismological observations, Science, 321, 1478-1481, 10.1126/science.1160943, 2008.

Chen, K., Dejoie, C., and Wenk, H.-R.: Unambiguous indexing of trigonal crystals from white-beam Laue diffraction patterns: application to Dauphiné twinning and lattice stress mapping in deformed quartz, J. Appl. Crystallogr., 45, 982-989, 10.1107/S0021889812031287, 2012.

IST 11/1/18 14:49
Supprimé: .

Chen, K., Kunz, M., Tamura, N., and Wenk, H.-R.: Residual stress preserved in quartz from the San Andreas Fault Observatory at Depth, Geology, 43, 219-222, 2015.

Chester, F. M., and Chester, J. S.: Ultracataclasite structure and friction processes of the Punchbowl fault, San Andreas system, California, Tectonophysics, 295, 199-221, 1998.

Cho, M., Maruyama, S., and Liou, J. G.: An experimental investigation of heulandite-laumontite equilibrium at 1000 to 2000 bar Pfluid, Contrib. Mineral. Petr., 97, 40-50, 1987.

Cummings, D.: Kink-bands : shock deformation of biotite resulting from a nuclear explosion, Science, 148, 950-952, 1965.

Dejoie, C., Kunz, M., Tamura, N., Bousige, C., Chen, K., Teat, S., Beavers, C., and Baerlocher, C.: Determining the energy-dependent X-ray flux variation of a synchrotron beamline using Laue diffraction patterns, J. Appl. Crystallogr., 44, 177-183, 10.1107/S0021889810052015, 2011.

Derez, T., Pennock, G., Drury, M., and Sintubin, M.: Low-temperature intracrystalline deformation microstuctures in quartz, J. Struct. Geol., 71, 3-23, 10.1016/j.jsg.2014.07.015, 2015.

Diamond, L. W., and Tarantola, A.: Interpretation of fluid inclusions in quartz deformed by weak ductile shearing : reconstruction of differential stress magnitudes and pre-deformation fluid properties, Earth Planetary Sc. Lett., 417, 107-119, 2015.

Dieter, G. E.: Mechanical metallurgy, Material Science and Engineering Series, McGraw-Hill, Inc., 774 pp., 1961.

Doan, M. L., and Gary, G.: Rock pulverization at high strain rate near the San Andreas fault, Nat. Geosci., 2, 709-712, 2009.

Dor, O., Ben-Zion, Y., Rockwell, T. K., and Brune, J.: Pulverized rocks in the Mojave section of the San Andreas Fault Zone, Earth Planetary Sc. Lett., 245, 642-654, 2006.

Dor, O., Chester, J. S., Ben-Zion, Y., Brune, J. N., and Rockwell, T. K.: Characterization of damage in sandstones along the Mojave Section of the San Andreas Fault: implications for the shallow extent of damage generation, Pure Appl. Geophys., 166, 1747-1773, 2009.

Fabbri, O., Iwamura, K., Matsunaga, S., Coromina, G., and Kanaori, Y.: Distributed strike-slip faulting, block rotation, and possible intracrustal vertical decoupling in the convergent zone of southwest Japan, in: Vertical Coupling and Decoupling of the Lithosphere, edited by: Grocott, J., Tikoff, B., McCaffrey, K. J. W., and Taylor, G., Geol. Soc. Spec. Publ.,, 227, 141–166, 2004.

Famin, V., Raimbourg, H., Garcia, S., Bellahsen, N., Hamada, Y., Boullier, A.-M., Michon, L., Revil, A., Uchide, T., Ricci, T., Hirono, T., and Kawabata, K.: Stress rotations and the long-term weakness of the Median Tectonic Line and the Rokko-Awaji segment, Tectonics, 33, 1900-1919, 10.1002/2014TC003600, 2014.

Fauré, J.: Recherches sur les effets géologiques d'explosions atomiques souterraines dans un massif de granite saharien, Faculté des Sciences, Université de Nancy, 433 pp., 1970.

Fujimoto, K., Ueda, A., Ohtani, T., Takahashi, M., Ito, H., Tanaka, H., and Boullier, A. M.: Borehole water and hydrologic Nojima fault, SW model around the Japan, Tectonophysics, 443, 174-182, 2007.

Hickman, S., and Zoback, M.: Stress orientations and magnitudes in the SAFOD pilot hole, Geophys. Res. Lett., 31, L15S12, 10.1029/2004GL020043, 2004.

Hielscher, R., and Schaeben, H.: A novel pole figure inversion method: specification of the MTEX algorithm, J.Appl. Crystallogr., 41, 1024-1037, 10.1107/S0021889808030112, 2008.

Hilgers, C., Köhn, D., Bons, P. D., and Urai, J. L.: Development of crystal morphology during unitaxial growth in a progressive widening vein: II. Numerical simulations of the evolution of antitaxial fibrous veins, J. Struct. Geol., 23, 873-885, 2001.

Hirth, G., and Tullis, J.: The brittle-plastic transition in experimentally deformed quartz aggregates, J. Geophys. Res., 99, 11731-11747, 1994.

Ikeda, R., Iio, Y., and Omura, K.: In situ stress measurements in NIED boreholes in and around the fault zone near the 1995 Hyogo-ken Nanbu earthquake, Japan, Isl. Arc, 10, 252-260, 2001.

Ito, H., Kuwahara, Y., Kiguchi, T., Fujimoto, K., and Ohtani, T.: Outline of the Nojima Fault drilling by GSJ : structure, physical properties and permeability structure from borehole measurements in GSJ borehole crossing the Nojima Fault, Japan, Proceedings of the International workshop on the Nojima fault core and borehole analysis, Tsukuba, Japan, 1999, 71-79, 2000.

Kanaori, Y.: Late Mesozoic-Cenozoic strike-slip and block rotation in the inner belt of Southwest Japan, Tectonophysics, 177, 381-399, 1990.

Kunz, M., Chen, K., Tamura, N., and Wenk, H.-R.: Evidence for residual elastic strain in deformed natural quartz, Am. Mineral., 94, 1059-1062, 2009.

Lin, W., Kwasniewski, M., Imamura, T., and Matsuki, K.: Determination of three-dimensional in situ stresses from anelastic strain recovery measurements of cores at great depth, Tectonophysics, 426, 221-238, 2006.

Lloyd, G. E.: Grain boundary contact effects during faulting of quartzite: an SEM/EBSD analysis, J. Struct. Geol., 22, 1675-1693, 2000.

Lloyd, G. E.: Microstructural evolution in a mylonitic quartz simple shear zone : the significant roles of Dauphiné twinning and misorientation, in: Flow processes in faults and shear zones, edited by: Alsop, G. I., Holdswoorth, R. E., McCaffrey, K. J. W., and Hand, M., Geol. Soc. Spec. Publ.,, 224, 39-61, 2004.

Lockner, D. A., Tanaka, H., Ito, H., Ikeda, R., Omura, K., and Naka, H.: Geometry of the Nojima Fault at Nojima-Hirabayashi, Japan - I. A Simple Damage Structure Inferred from Borehole Core Permeability, Pure Appl. Geophys., 166, 1649-1667, 2009.

Mainprice, D., Bachmann, F., Hielscher, R., and Schaeben, H.: Descriptive tools for the analysis of texture projects with large datasets using MTEX: strength, symmetry and components, in: Rock Deformation from Field, Experiments and Theory: A Volume in Honour of Ernie Rutter, edited by: Faulkner, D. R., Mariani, E., and Mecklenburgh, J., Geol. Soc. Spec. Publ.,, 409, 251-271, 2014.

Mainprice, D., Lloyd, G. E., and Casey, M.: Individual orientation measurements in quartz polycrystals - Advantages and limitations for texture and petrophysical property determinations, J. Struct. Geol., 15, 1169-1187, 1993.

Menegon, L., Piazolo, S., and Pennacchioni, G.: The effect of Dauphiné twinning on plastic strain in quartz, Contrib. Mineral. Petr, 161, 635-652, 2011.

Mitchell, T. M., Ben-Zion, Y., and Shimamoto, T.: Pulverized fault rocks and damage asymmetry along the Arima-Takatsuki Tectonic Line, Japan, Earth Planetary Sc. Lett., 308, 284-297, 10.1016/j.epsl.2011.04.023, 2011.

Murakami, M., and Tagami, T.: Dating pseudotachylyte of the Nojima fault using the zircon fission-track method, Geophys. Res. Lett., 31, L12604, 10.1029/2004GL020211, 2004.

Nédélec, A., and Bouchez, J.-L.: Pétrologie des granites : structure, cadre géologique, Interactions, edited by: De Wever, P., Société Géologique de France, Vuibert, Paris, 306 pp., 2011.

Nicolas, A., and Poirier, J.-P.: Crystalline plasticity and solid-state flow in metamorphic rocks, J. Wiley Interscience Publications, London, 444 pp., 1976.

Ogi, H., Ohmori, T., Nakamura, N., and Hirao, M.: Elastic, anelastic, and piezoelectric coefficients of α-quartz determined by resonnance ultrasound spectroscopy, J. Appl. Phys., 100, 053511, 2006.

Ohtani, T., Fujimoto, K., Ito, H., Tanaka, H., Tomida, N., and Higuchi, T.: Fault rocks and past to recent fluid characteristics from the borehole survey of the Nojima fault ruptured in the 1995 Kobe earthquake, southwest Japan, J. Geophys. Res., 105, B7, 16161-16171, 2000a.

Ohtani, T., Miyazaki, T., Tanaka, H., Kiguchi, T., Fujimoto, K., and Ito, H.: Reorientation of cores and distribution of macroscopic fractures along the GSJ borehole penetrating the Nojima fault zone, International workshop of the Nojima fault core and borehole data analysis, Tsukuba, Japan, 1999, 271-276, 2000b.

Pêcher, A.: Experimental decrepitation and reequilibration of fluid inclusions in synthetic quartz, Tectonophysics 78, 567-584, 1981.

Pehl, J., and Wenk, H.-R.: Evidence for regional Dauphiné twinning in quartz from the Santa Rosa mylonite zone in Southern California. A neutron diffraction study, J. Struct. Geol., 27, 1741–1749, 2005.

Petit, J., Castelnau, O., Bornert, M., Zhang, F. G., Hofmann, F., Korsunsky, A. M., Faurie, D., Le Bourlot, C., Micha, J. S., Robach, O., and Ulrich, O.: Laue-DIC: a new method for improved stress field measurements at the micrometer scale, J. Synchrotron Radiat., 22, 980–994, 10.1107/S1600577515005780, 2015.

Reches, Z., and Dewers, T. A.: Gouge formation by dynamic pulverization during earthquake rupture, Earth Planetary Sc. Lett., 235, 361-374, 10.1016/j.epsl.2005.04.009, 2005.

Robach, O., Micha, J.-S., Ulrich, O., Devincre, B., Hoc, T., Daveau, G., Consonni, V., and Petit, J.: Analyse avancée des des contraintes et des gradients d'orientation par microdiffraction Laue des rayons X, in: Rayons X et Matière 5, RX2013, edited by: Guinebretière, R., and Goudeau, P., ISTE Editions, 83-147, 2017.

Rockwell, T., Sisk, M., Girty, G., Dor, O., Wechsler, N., and Ben-Zion, Y.: Chemical and Physical Characteristics of Pulverized Tejon Lookout Granite Adjacent to the San Andreas and Garlock Faults: Implications for Earthquake Physics, Pure Appl. Geophys., 166, 1725-1746, 2009.

Roedder, E.: Fluid inclusions, Reviews in Mineralogy, 12, Mineral. Soc. Am., 644 pp., 1984.

Rosakis, A. J., Xia, K., Lykotrafitis, G., and Kanalori, H.: Dynamic shear rupture in frictional interfaces: speeds, directionality, and modes, in: Treatise of Geophysics, Elsevier, 153-192, 2007.

Sagy, A., and Korngreen, D.: Dynamic branched fractures in pulverized rocks from a deep borehole, Geology, 40, 799-802, 2012.

Savage, J. C., and Wood, M. D.: The relation between apparent stress and stress drop, B. Seismol. Soc. Am., 61, 1381–1388, 1971.

Shamir, G., and Zoback, M. D.: Stress orientation profile to 3.5 km depth near the San Andreas Fault at Cajon Pass, California, J. Geophys. Res., 97, 5059-5080, 1992.

Sherby, O. D., Klundt, H. R., and Miller, A. K.: Flow stress, subgrain size, and subgrain stability at elevated temperature, Metall. Trans. A, 8, 843-850, 1977.

Shi, Z., and Ben‐Zion, Y.: Dynamic rupture on a bimaterial interface governed by slip‐weakening friction, Geophys. J. Int., 165, 469–484, 10.1111/j.1365‐246X.2006.02853.x, 2006.

Sibson, R. H.: Fault rocks and fault mechanisms, J. Geol. Soc. London, 191-213, 1977.

Sibson, R. H.: Thickness of the seismic slip zone, B. Seismol. Soc. Am., 93, 1169-1178, 2003.

Stünitz, H., Thust, A., Heilbronner, R., Behrens, H., Kilian, R., Tarantola, A., and Fitz Gerald, J. D.: Water redistribution in experimentally deformed natural milky quartz single crystals—Implications for H2O-weakening processes, J. Geophys. Res.-Sol. Ea., 122, 866–894, 10.1002/2016JB013533, 2017.

Sullivan, W. A., and Peterman, E. M.: Pulverized granite at the brittle-ductile transition: an exemple from the Kellyland fault zone, eastern Maine, U.S.A., J. Struct. Geol., 101, 109-123, 10.1016/j.jsg.2017.07.002, 2017.

Tamura, N.: XMAS : a versatile tool for analyzing synchrotron X-ray microdiffraction data, in: Strain and dislocation gradients from diffraction, edited by: Barabash, R. I., and Ice, G. E., Imperial College Press / World Scientific Publishing, 125-155, 2014.

Tanaka, H., Fujimoto, K., Ohtani, T., and Ito, H.: Structural and chemical characterization of shear zones in the freshly activated Nojima fault, Awaji Island, southwest Japan, J. Geophys. Res., 106, 8789–8810, 2001.

Tarantola, A., Diamond, L. W., and Stunitz, H.: Modification of fluid inclusions in quartz by deviatoric stress I: experimentally induced changes in inclusion shapes and microstructures, Contrib. Mineral. Petr, 160, 825-843, 2010.

Trepmann, C. A.: Shock effects and pre-shock microstructures in hydrothermal quartz veins from the Rochechouart impact structure, France, J. Struct. Geol., 31, 1183-1196, 0.1016/j.jsg.2009.06.017, 2009.

Trepmann, C. A., Hsu, C., Hentschel, F., Döhler, K., Schneider, C., and Wichmann, V.: Recrystallization of quartz after low-temperature plasticity - The record of stress relaxation below the seismogenic zone, J. Struct. Geol., 95, 72-92, 10.1016/j.jsg.2016.12.004, 2017.

Trepmann, C. A., and Stöckert, B.: Cataclastic deformation of garnet : a record of synseismic loading and postseismic creep, J. Struct. Geol., 24, 1845-1856, 2002.

Trepmann, C. A., and Stöckert, B.: Short-wavelength undulatory extinction in quartz recording coseismic deformation in the middle crust – an experimental study, Solid Earth, 4, 263-276, 10.5194/se-4-263-2013, 2013.

Tullis, J.: Deformation of granitic rocks : experimental studies and natural examples, in: Plastic deformation of minerals and rocks, edited by: Karato, S.-I., and Wenk, H.-R., Rev. Mineral. Geochem., 51, Mineral. Soc. Am., Geochem. Soc., 51-95, 2002.

Ulrich, O., Biquard, X., Bleuet, P., Geaymond, O., Gergaud, P., Micha, J. S., Robach, O., and Rieutord, F.: A new white beam X-ray microdiffraction setup on the BM32 beamline at the European Synchrotron Radiation Facility, Rev. Sci. Instrum., 82, 033908, 2011.

Wechsler, N., Allen, E. E., Rockwell, T. K., Girty, G., Chester, J. S., and Ben-Zion, Y.: Characterization of pulverized granitoids in a shallow core along the San Andreas Fault, Littlerock, CA, Geophys. J. Int., 186, 401-417, 0.1111/j.1365-246X.2011.05059.x, 2011.

Wenk, H.-R., Janssen, C., Kenkmann, T., and Dresen, G.: Mechanical twinning in quartz : shock experiments, impact, pseudotachylites and fault breccias, Tectonophysics, 510, 69-79, 2011.

Wenk, H.-R., Lonardelli, I., Vogel, S. C., and Tullis, J.: Dauphiné twinning as evidence for an impact origin of preferred orientation in quartzite ; an example from Vredefort, South Africa, Geology, 33, 273-276., 2005.

Wenk, H.-R., Rybacki, E., Dresen, G., Lonardelli, I., Barton, N., Franz, H., and Gonzalez, G.: Dauphiné twinning and texture memory in polycrystalline quartz. Part 1: Experimental deformation of novaculite, Phys. Chem. Miner., 33, 667-676, 2006.

Xia, K., Nasseri, M. H. B., Mohanty, B., Lu, F., Chen, R., and Luo, S. N.: Effects of microstructures on dynamic compression of Barre granite, Int. J. Rock Mech. Min., 45, 879-887, 2008.

Yuan, F., Prakash, V., and Tullis, T.: Origin of pulverized rocks during earthquake fault rupture, J. Geophys. Res.- Sol. Ea., 16, B06309, 10.1029/2010JB007721, 2011.

Zamora, M., Pézard, P. A., and Ito, H.: Anisotropy of elastic and anelastic properties of granites from the Hirabayashi hole, Japan, International workshop of the Nojima fault core and borehole data analysis, Tsukuba, Japan, 1999, 227-231, 2000.

Zhang, Q. B., and Zhao, J.: A review of dynamic experimental techniques and mechanical behaviour of rock materials, Rock Mech. Rock Eng., 10.1007/s00603‐013‐0463‐y, 2013.

Zoback, M. D., and Healy, J. H.: In situ measurements to 3.5 km depth in the Cajon Pass scientific research borehole: implications for the mechanics of crustal faulting, J. Geophys. Res., 97, 5039-5057, 1992.

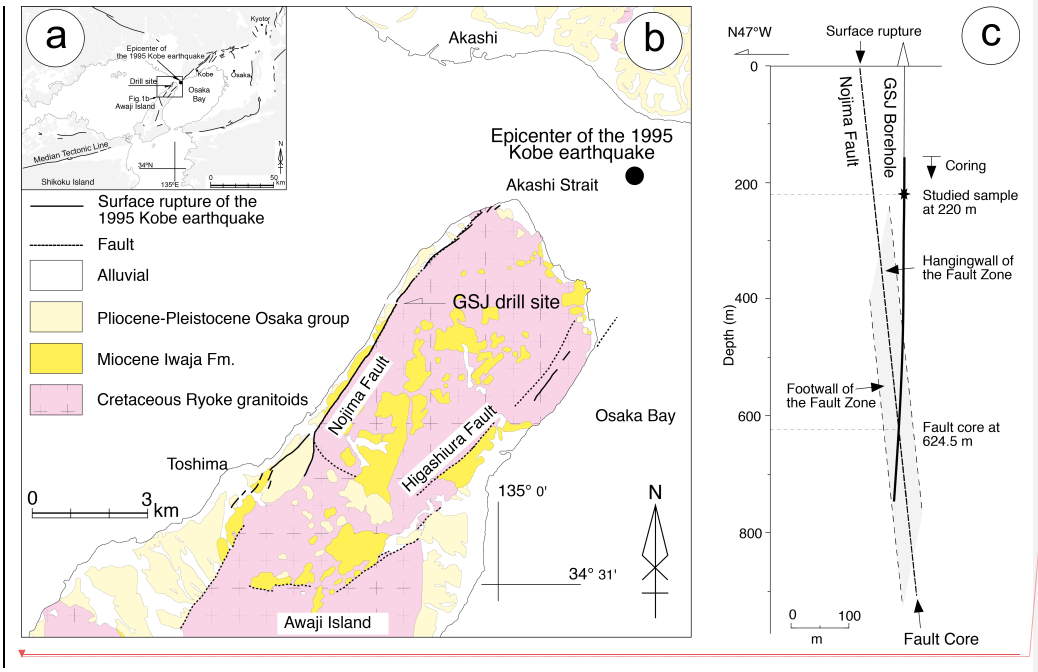

Figure 1 : Geological setting (modified from Ohtani et al., 2000a). a) Insert showing the localization of the Awaji Island. b) Geological map of the Awaji Island showing the Nojima fault and the location of the GSJ Hirabayashi drillhole. c) Schematic cross-section showing the relative geometries of the Nojima fault and the GSJ drillhole.

IST 10/1/18 15:13
Surface rupture at the 1995 Kobe earthquake
Fault
Flexure
Alluvial
Pliocene-Pleistocene O
Miocene Iwaja Fm.
Cretaceous granitoids
GSJ c
0
5
km
N
Toshima
Supprimé:

IST 11/1/18 14:43
Supprimé: .

IST 11/1/18 14:39
Supprimé: (modified from Ohtani et al., 2000a).

IST 11/1/18 14:43
Supprimé: b

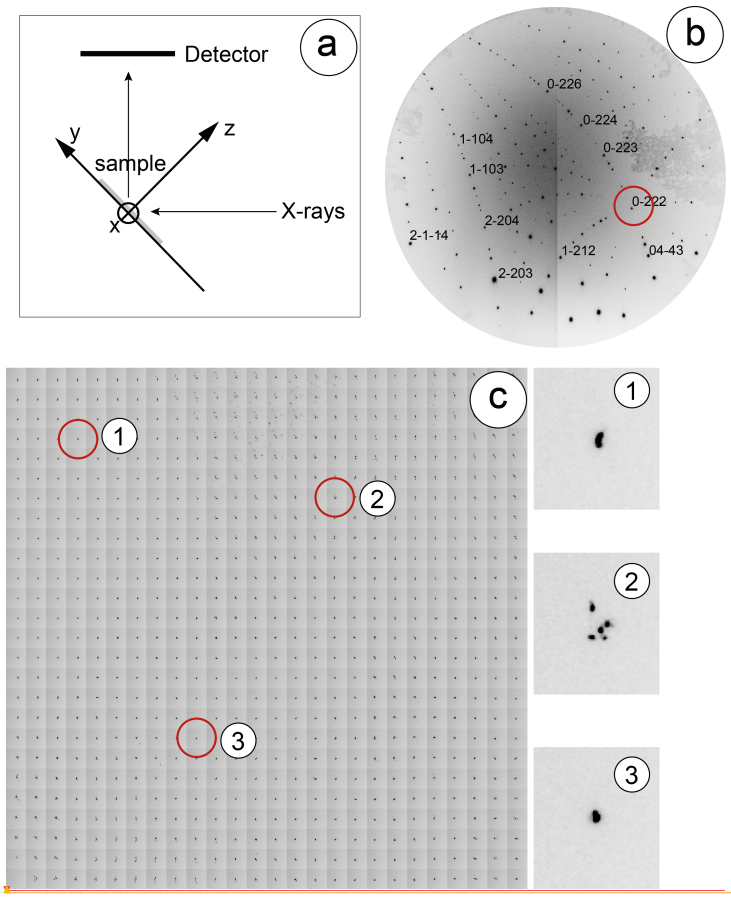

Figure 2 : X-ray Laue microdiffraction. a) Geometric disposition of the sample relative to the X-rays beam and definition of the x, y and z axes of the sample referential. A more detailed definition of the sample reference frame is provided in Petit et al. (2015). b) Laue image corresponding to the point indicated by the red circle 3 on the map ; some spots are indexed, especially the (0-222) spot (red circle) which has been used for the following mosaic map. The detector image is oriented as the one that would be seen by an observer lying at the place of the sample and receiving the incident beam on the top of the head. c) 26 x 26 points mosaic map constructed with a 10 µm step on the quartz grain analyzed in Figure 4. The (0-222) spot location, shape and intensity on the detector vary on each step depending on the orientation, crystallinity and deformation of the crystal. In the point 2 of the map, multiple spots are indicative of several subgrains present in the analyzed volume; in point 1, the (0-222) spot is elongated in a NNW-SSE direction indicating a continuous bending of the crystal lattice roughly around the x axis (Robach et al., 2017).

IST 5/3/18 10:33
Supprimé:
Unknown
Mis en forme: Police :(Par défaut)
IST 9/3/18 11:21
Supprimé: –Laue

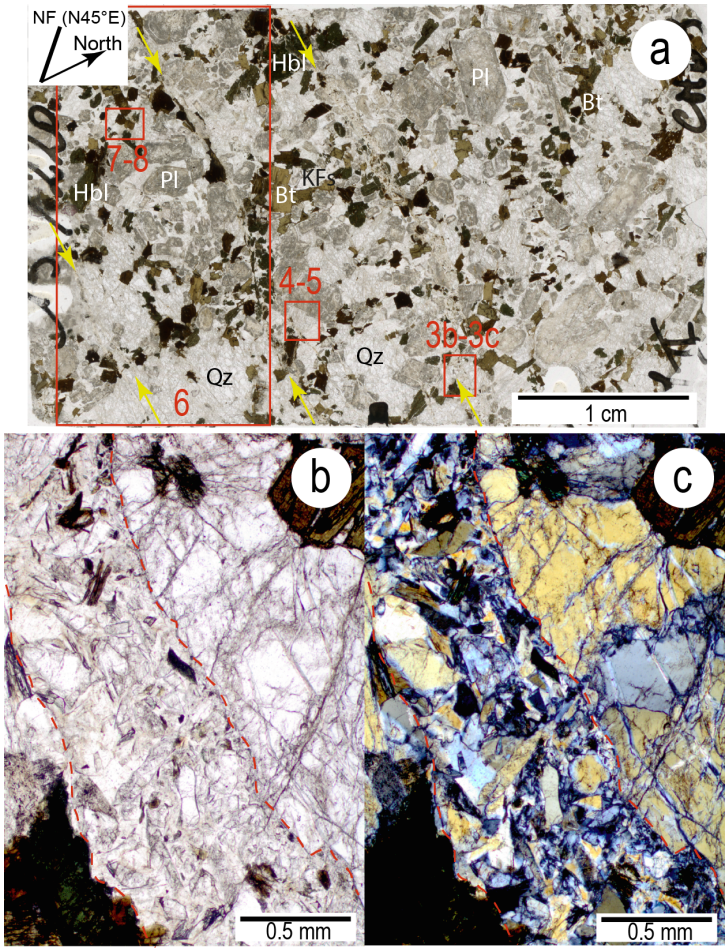

Figure 3 : The NOJ220 thin section (45 x 30 mm). a) Scan showing the overall preserved magmatic texture. The orientation of the thin section is inverse and indicated in the top left box (NF : Nojima fault). Brown to black minerals are biotites (Bt) or hornblendes (Hbl). Greyish large minerals are K-feldpars (Kfs) or plagioclases (Pl). Light grey minerals are micro-fractured quartz (Qz). Red rectangles localize Figure 3b, 3c, 4a, 6, 7 and 8. Yellow arrows indicate breccia-like laumontite-filled veins. b) and c) Microphotographs in plane polarized light (b) and crossed polarized light (c) of a breccia-like laumontite-filled vein showing the angulous mineral fragments within a laumontite matrix. The red dotted lines locate the vein walls.

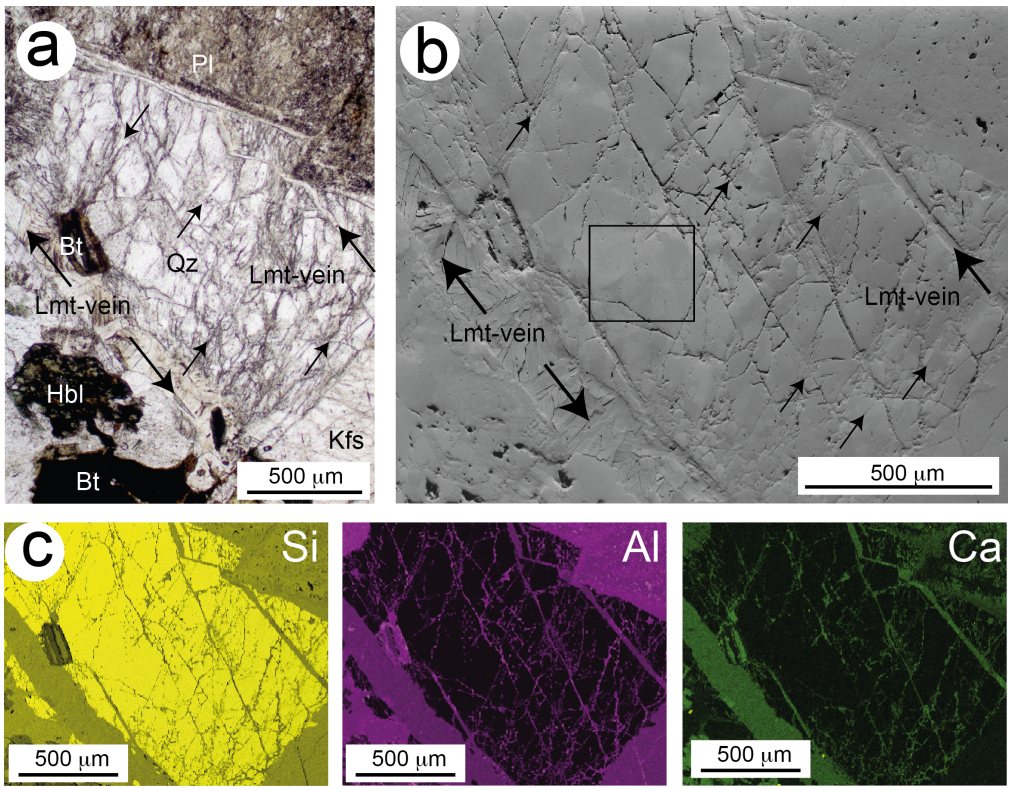

Figure 4 : Representative quartz grain (Qz) studied with EBSD (area shown on Fig. 3a). a) Microphotograph (plane polarized light) of the quartz grain bound by laumontite (Lmt) veins (large black arrows) and surrounded by K-feldspar (Kfs), plagioclase (Pl), biotite (Bt) and hornblende (Hbl). The quartz grain shows abundant well orientated intragranular microfractures (small black arrows). b) Forward-scattered electron image of the same area. Thick arrows : intergranular laumontite-filled veins. Thin arrows : intragranular microfractures and alignments of tiny fluid inclusions. The slightly different grey levels are due to different crystallographic orientations. The rectangle locates the sub-region finely mapped with EBSD (Figure 10) and X-ray Laue microdiffraction (Figure 11). c) Compositional maps of the same area for Si, Ca and Al showing the laumontite-filled veins.

IST 9/3/18 11:27
Supprimé: 8

IST 9/3/18 11:27
Supprimé: Laue

IST 9/3/18 11:27
Supprimé: 9

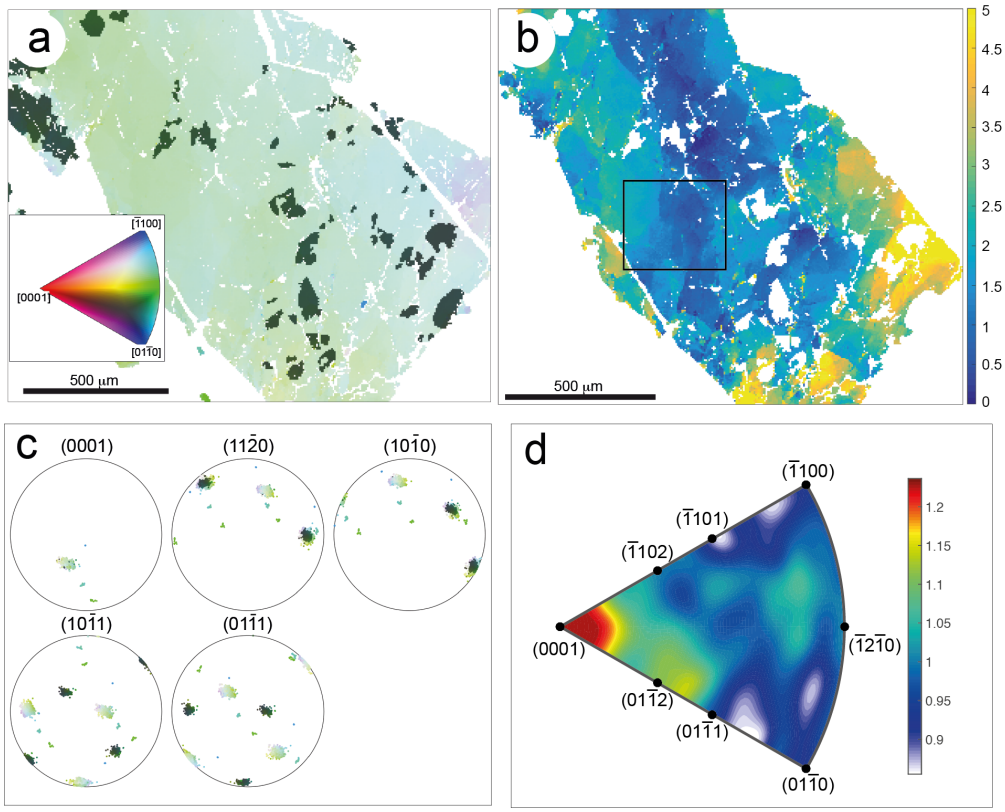

Figure 5 : EBSD measurements on the quartz grain shown in Figure 4. a) Crystallographic orientation map measured by EBSD. The Inverse Pole Figure (IPF) colouring indicates the orientation of each pixel relative to the horizontal axis of the map. The dark green patches correspond to Dauphiné twinned domains defined by a 60° rotation around the [0001] axis. b) Misorientation map relative to the mean orientation of the quartz grain (excluding Dauphiné twins) with misorientations up to 5°. The rectangle indicates the area studied in Figure 10. c) Pole figures of the principal crystallographic axes of quartz using the same colour code as in a). Upper hemisphere projection. d) Inverse pole figure of rotation axes that correspond to misorientations between 0.5 and 5°. Colour scale : multiple of uniform distribution.

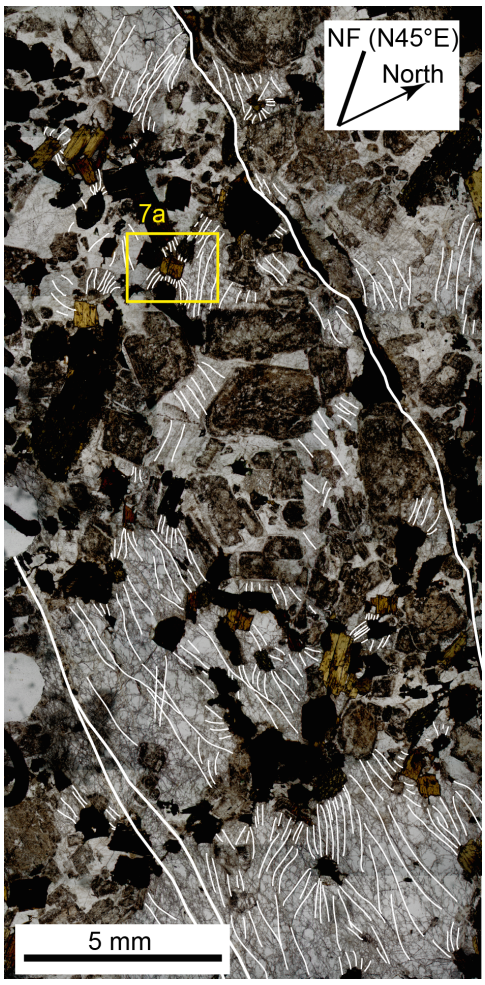

Figure 6 : Schematic drawing on the NOJ220 thin section showing an array of numerous microfractures (thin white lines) joining one biotite or hornblende to another on the entire thin section width. The thicker white line indicates one breccia-like laumontite vein (see Fig. 3a for location). The yellow rectangle localizes the area studied in Figures 7 and 8. The orientation of the thin section is inverse and indicated in the top left box (NF : Nojima fault).

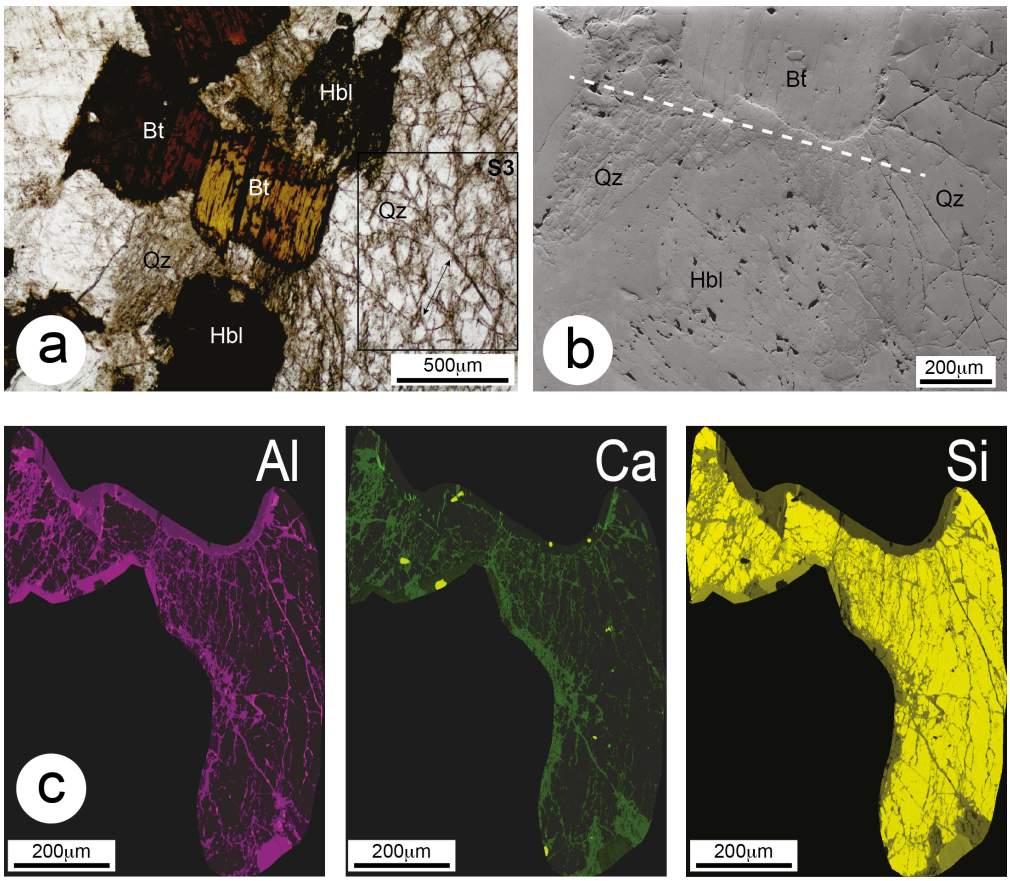

Figure 7 : Microstructures in the area shown in Fig. 3a. a) Quartz grains squeezed between a biotite (Bt) and a hornblende (Hbl) and displaying intensive microfracturing. The small black arrow on the right indicates the preferred orientation of the alignments of tiny fluid inclusions in quartz (compare with Figure 4a). b) Forward-scattered electron image of the same area. The slightly different grey levels in quartz are due to different crystallographic orientations. The white dashed line locates the transect on which a 30% dilatancy has been measured. c) Compositional maps of the same area for Si, Ca and Al showing the laumontite-filled veins.

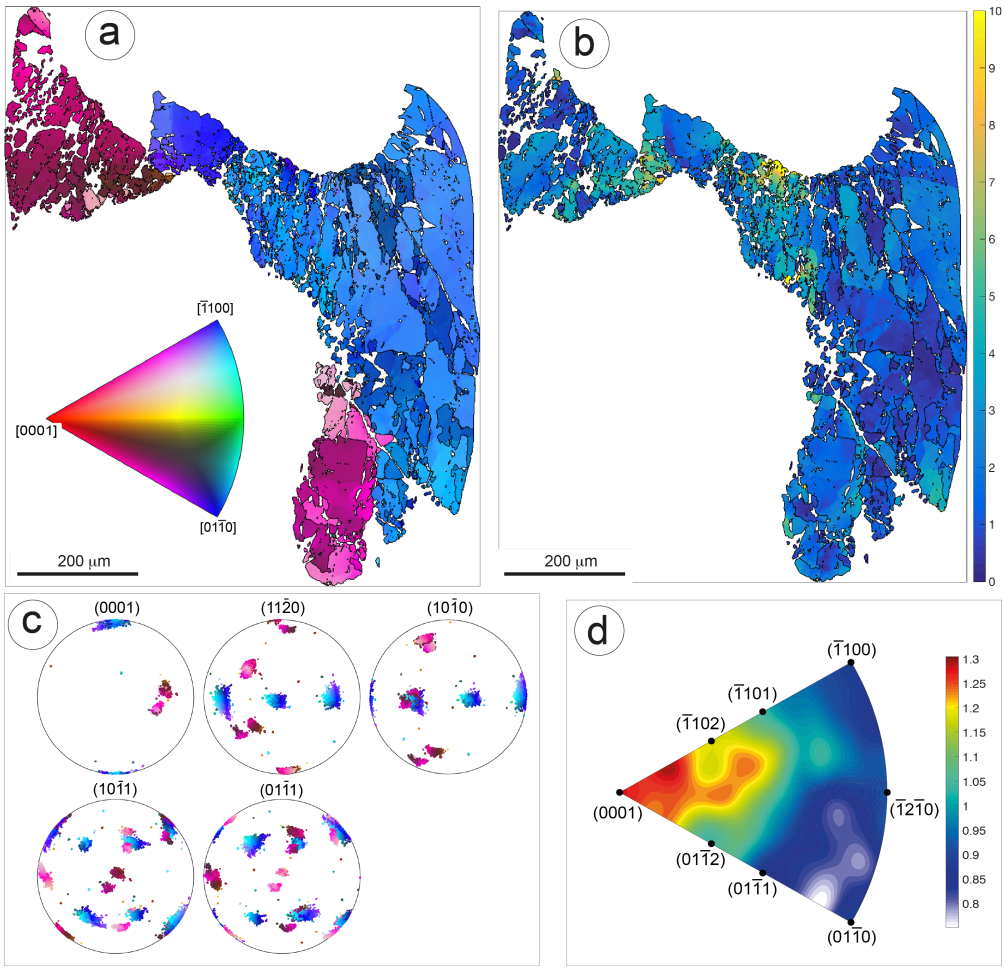

Figure 8 : EBSD measurements on the quartz grains shown in Figure 7. a) Orientation map ; the colour scale indicates the minimum angle between each pixel and the reference orientation defined by (0, 0, 0) Euler angles. b) Misorientation map relative to the mean orientation of each quartz grain with misorientations up to 10°. c) Pole figures of the principal crystallographic axes of the three quartz grains using the same colour code as in a). Upper hemisphere projection. d) Inverse pole figure of rotation axes that correspond to misorientations between 0.5 and 10°. Colour scale : multiple of uniform distribution.

IST 26/1/18 12:21
Supprimé:

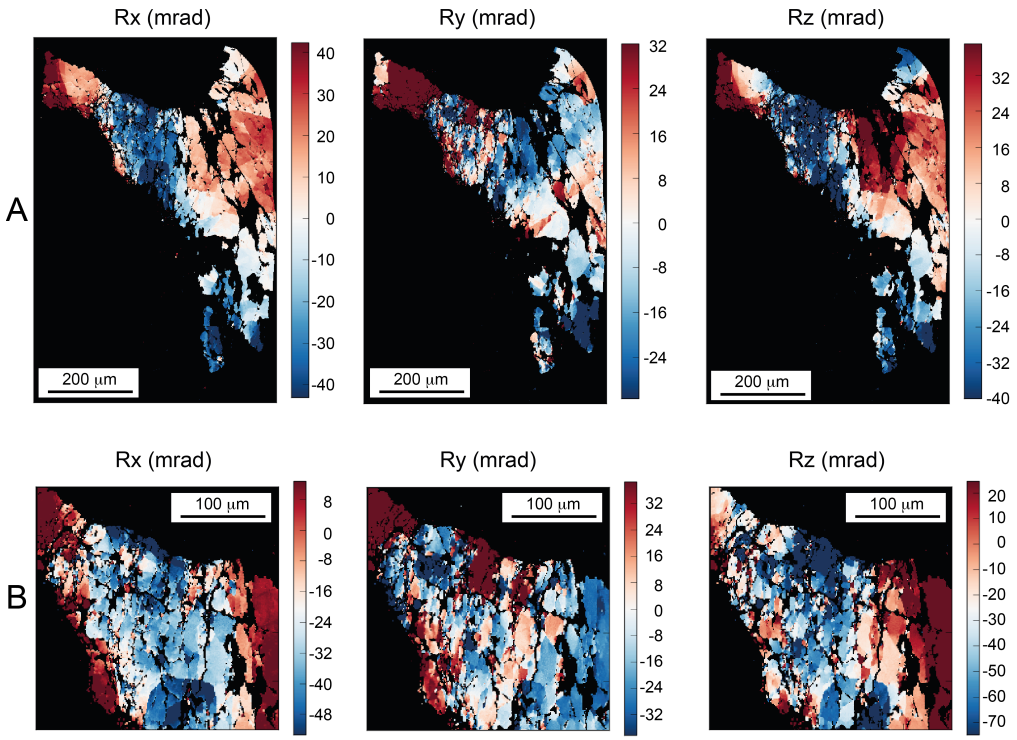

Figure 9 – Maps of the Rx, Ry and Rz rotations of the crystal lattice around the x, y and z axes (sample referential), in the region explored in Figure 8. Rx, Ry and Rz were calculated with LaueTools from the EBSD data of Figure 8. The x,y map positions and the Euler angles of the EBSD file were first transformed in order to adapt to the LaueTools (LT) reference frames. The corresponding transformations are described in Supplementary Material 4. Histograms of orientation matrix components were then built, for different rectangular regions in the map of figure 8a, in order to identify the frequency peaks associated to the blue crystallite in the center of the map, and to define the thresholds for selecting the map points belonging to this crystallite according to their crystallographic orientation. In figure 9A, all the non-black pixels have their a* vector within less than 245 mrad (14 degrees) of the x axis. These pixels were used to calculate the mean orientation matrix of the crystallite (used as the zero for rotations). The twinned regions appear in black, i.e. they were excluded from the crystallite. A) Rotation components for the right part of Figure 8a. B) Zoom on the top-center area of Figure 8a. Scales in mrad differ (in amplitude and offset) between the different maps, in order to enhance the contrast for each rotation component.

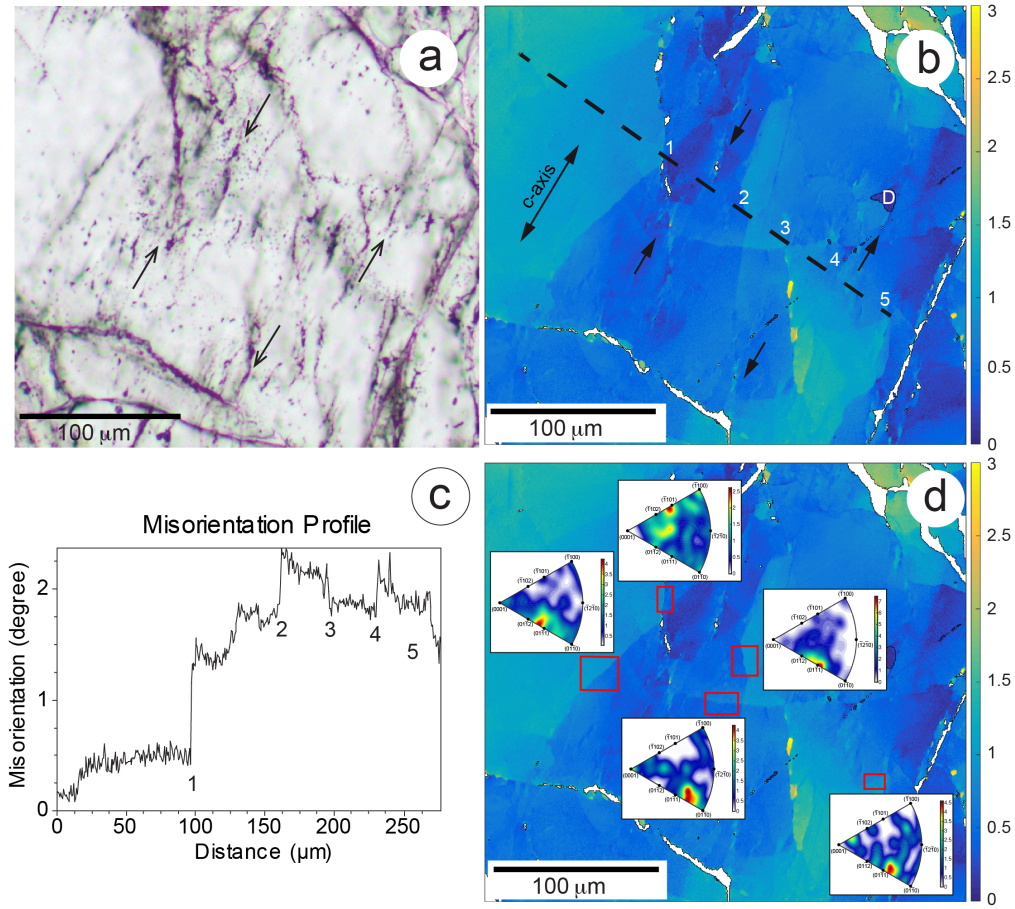

Figure 10 – EBSD measurements on the area shown in Figure 4b. a) Optical microphotograph showing the short microfractures (thin arrows) and alignments of tiny fluid inclusions. b) Map of misorientation of pixels relative to the mean orientation of the grain obtained by EBSD. The small dark domain (D) is a Dauphiné twinned domain. The projection of [0001] axis on the thin section plane is shown by the double black arrow. The short black arrows indicate the well orientated small elongated domains that could correspond to the short wavelength variations between subgrain boundaries or steps indicated as 1 to 5 on profile shown in b. c) Misorientation profile along the dashed line shown in b. d) Misorientation axes calculated for small areas across subgrain boundaries (red rectangles).

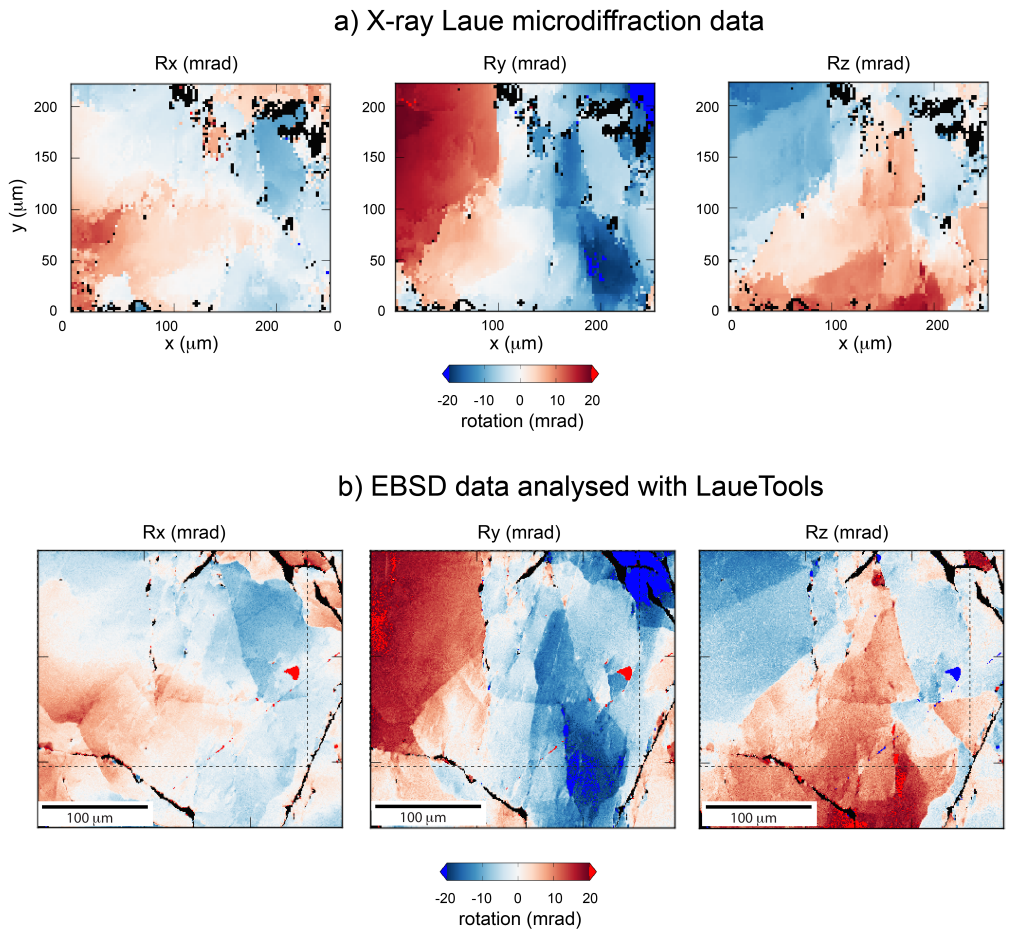

Figure 11 – Maps of the Rx, Ry and Rz rotations of the crystal lattice around the x, y and z axes (sample referential) relative to to the average orientation in each map in the small area described in Figure 10 and calculated using LaueTools. a) Rotations calculated from the X-ray Laue microdiffraction data. b) Rotations calculated from EBSD data. The dashed line indicates the area investigated using X-ray Laue microdiffraction. See Supplementary Material 4 for mathematical transformations applied to the EBSD data in order to pass the orientation matrices and map points positions into the LaueTools sample reference frame.

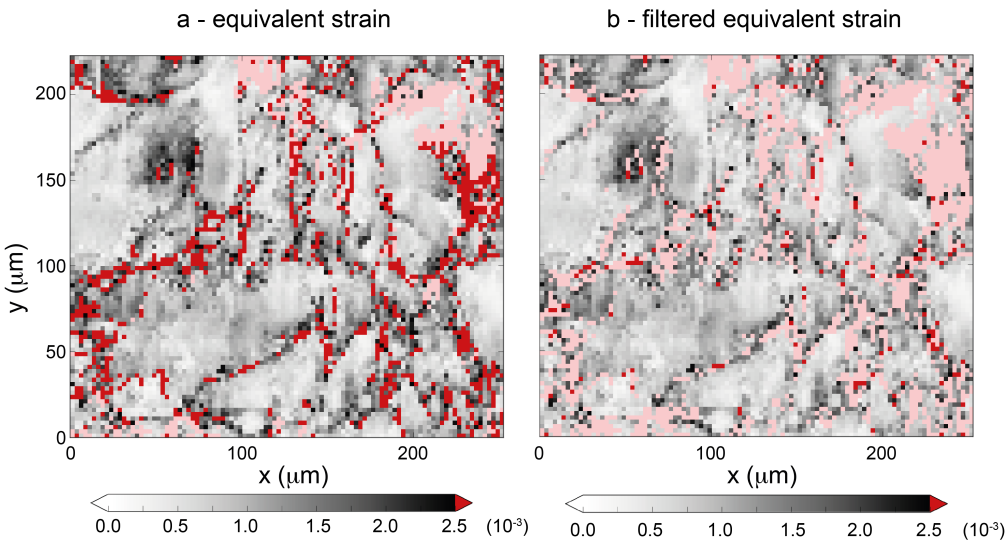

Figure 12 : Maps of the equivalent strain (see formula (1) in the main text) measured from the distorsion between the Laue pattern compared to the theoretical pattern of an undeformed crystal of the same orientation. a) Unfiltered data. Undetermined points are pink. b) Same data after filtering ; same scale as in a, filtered points in pink (7259 images remaining over 8989). Note that filtering eliminates almost all the points showing an equivalent strain greater than 2.5 e^{-3}.

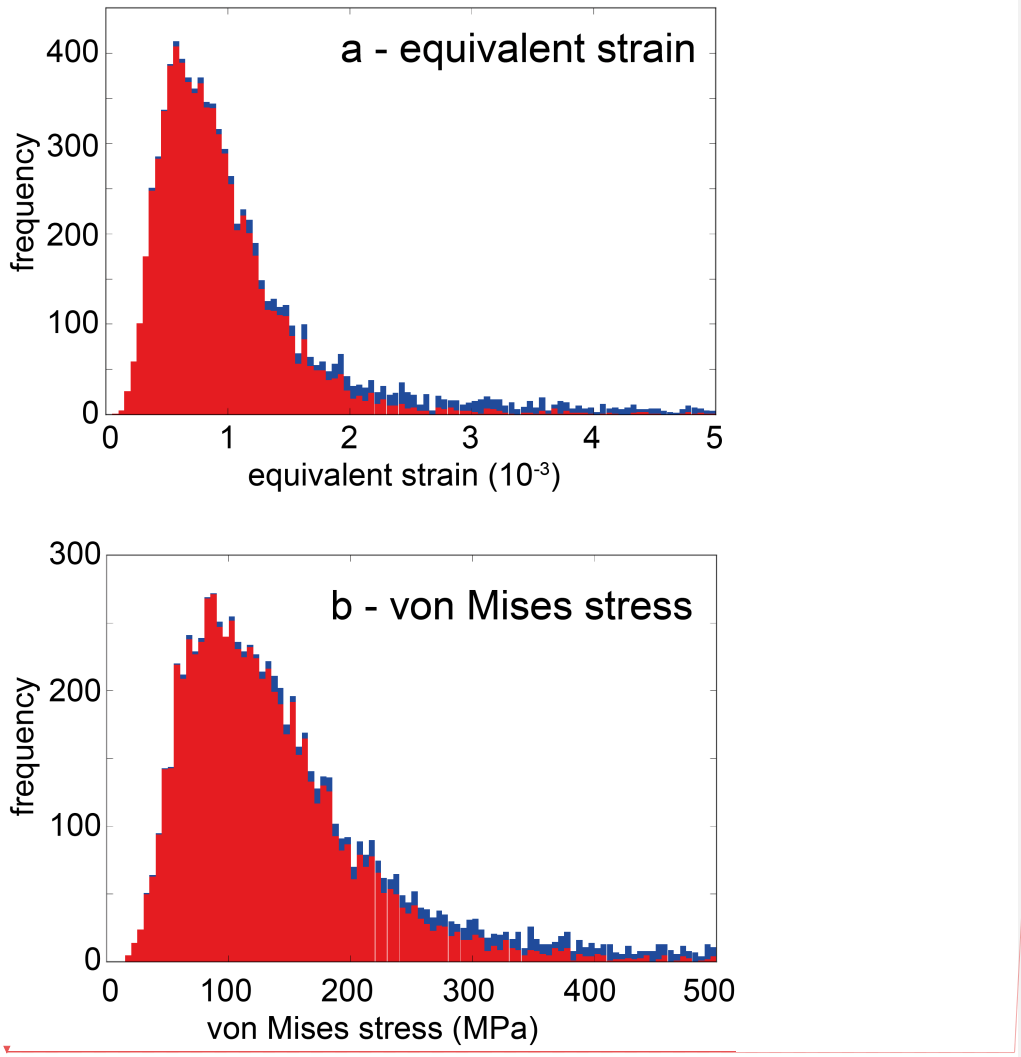

IST 10/1/18 15:18

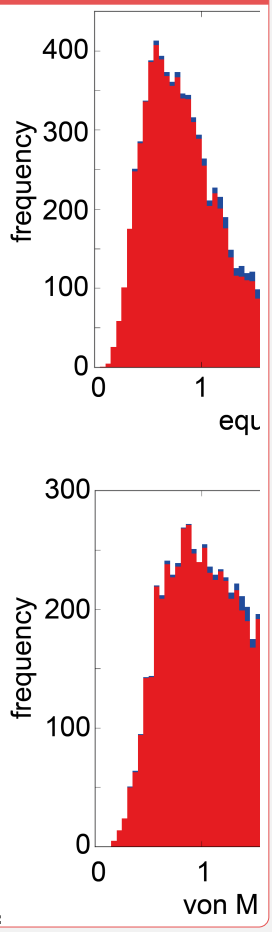

Supprimé:

Figure 13 : Distribution histograms of equivalent strain (a) and residual or von Mises stress values (b) without filtering (blue) or with filtering (red).

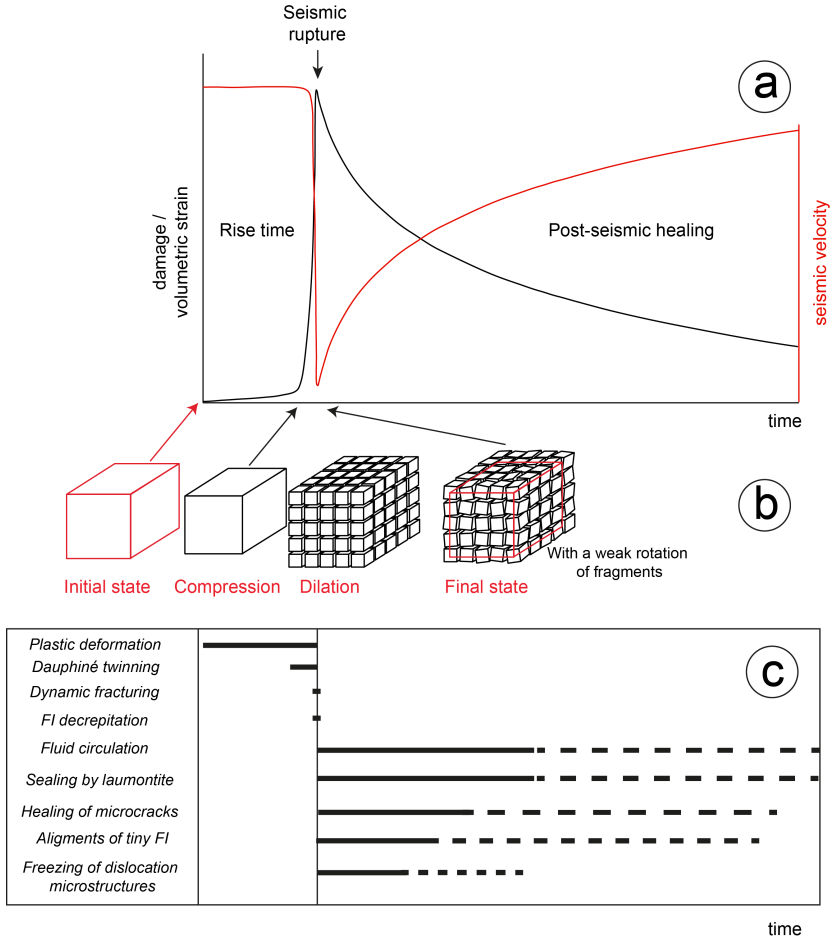

Figure 14 : Schematic interpretation showing the relationships between one characteristic earthquake and time of formation of the different microstructures observed in the NOJ220 sample. a) Variations of volumetric strain or damage versus time before and after a rupture. The red curve is drawn from the relative velocity changes observed by Brenguier et al. (2008) near Parkfield Parkfield (California) during three years after the M6 9/28/2004 Parkfield earthquake. b) Cartoon inspired by Reches and Dewers (2005) explaining the effect of a rupture front propagating on a fault. Successive compression and dilation (or dilation and compression) leads to fragmentation. c) Time and duration of formation of microstructures relative to the seismic rupture.

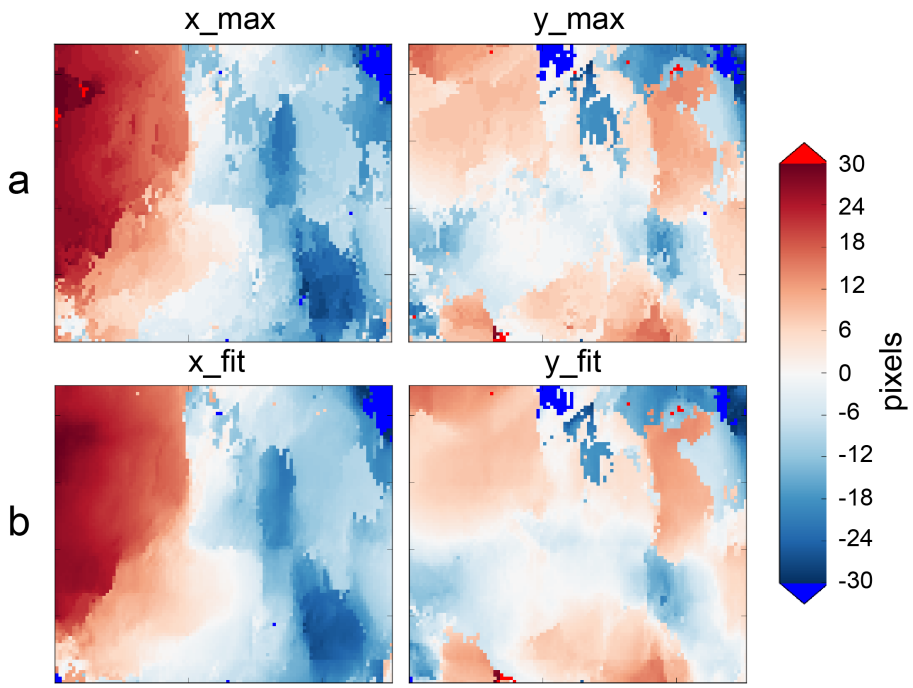

Figure A1 : X-ray Laue microdiffraction : one-spot analysis. Maps of the x,y pixel position of the (0-222) spot, for two different methods of calculation of this position. The mean position was subtracted. (a) xy_max (mean = 1476.43, 1211.59), (b) xy_fit (mean = 1476.65, 1211.45). See text of Appendix A1 for definition. The difference between (a) and (b) is mostly visible for M-type points, where several closely-space sub-grains are present in the beam path.

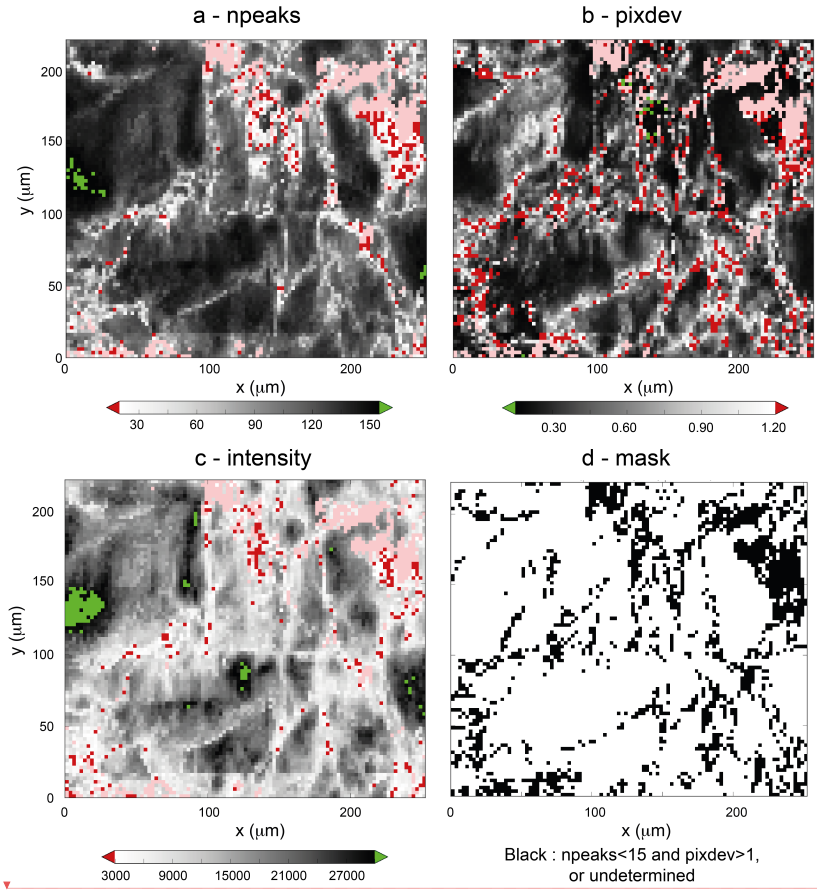

Figure A2 : Maps of three estimators (npeaks, pixdev, and intensity) of the local uncertainty on the shape / orientation of the unit cell, as calculated with the LaueTools software, and final mask used for removing "bad" data points (see explanations in the text). (a) : npeaks : number of Laue spots used for the refinement of the local orientation and deviatoric shape of the quartz unit cell. (b) : pixdev (mean pixel deviation) : estimator of the fit quality. (c) : intensity : average intensity of the 10 most intense spots of the Laue pattern of the grain. (d) : mask used for removing "bad" data points from strain maps, black pixels have npeaks < 25 or pixdev > 1. Pink points in Figure A2 a, b, c are points where the spot-link failed (missing points), and black points of the mask correspond to points either missing or with a npeaks below 25 or a mean pixdev above 1 pixel.

IST 11/1/18 10:55
Supprimé: . ... [7]

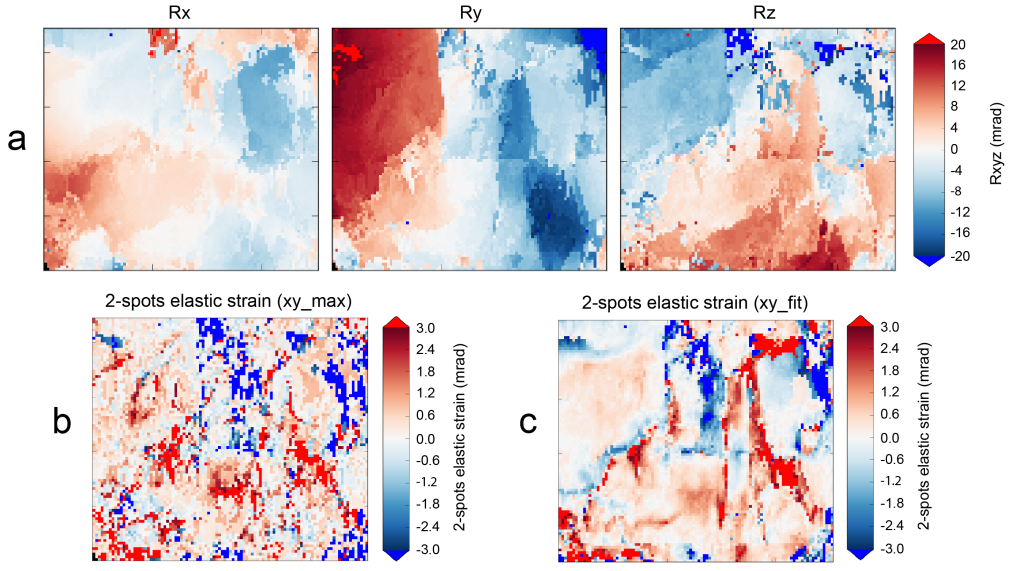

Unknown

Mis en forme: Police :10 pt, Non Gras

Figure A3 : X-ray Laue microdiffraction : two-spots analysis, using the xy_max position of the (0-222) and (2-203) spots. (a) lattice rotations with respect to the mean orientation, around the axes of the sample reference frame. (b) 2 spots elastic strain as measured from the angle between the reciprocal lattice vectors of the two spots (after subtracting the angle for unstrained quartz). (c) same as (b) using xy_fit. High strain map points (dalf > 5 mrad) are excluded when calculating the mean orientation matrix used in (a).